



Published in final edited form as:

Brain Stimul. 2021 ; 14(3): 549–563. doi:10.1016/j.brs.2021.03.009.

Image-Based Biophysical Modeling Predicts Cortical Potentials Evoked with Subthalamic Deep Brain Stimulation

Bryan Howell^a, Faical Isbaïne^b, Jon T. Willie^b, Enrico Opri^c, Robert E. Gross^b, Coralie De Hemptinne^d, Philip A. Starr^e, Cameron C. McIntyre^a, Svjetlana Miocinovic^c

^aDepartment of Biomedical Engineering, Case Western Reserve University

^bDepartment of Neurosurgery, Emory University

^cDepartment of Neurology, Emory University

^dDepartment of Neurology, University of Florida

^eDepartment of Neurological Surgery, University of California San Francisco

Corresponding Author: Svjetlana Miocinovic, svjetlana.miocinovic@emory.edu.

Author contributions

Bryan Howell: Conceptualization; Formal analysis; Investigation; Methodology; Software; Visualization; Roles/Writing - original draft; Writing - review & editing. **Cameron C. McIntyre:** Conceptualization; Funding acquisition; Methodology; Resources; Writing - review & editing. **Philip A. Starr:** Conceptualization; Funding acquisition; Resources; Writing - review & editing. **Svjetlana Miocinovic:** Conceptualization; Formal analysis; Funding acquisition; Investigation; Methodology; Project administration; Resources; Supervision; Visualization; Roles/Writing - original draft; Writing - review & editing. **All other authors:** Conceptualization, Writing - review & editing.

Publisher's Disclaimer: This is a PDF file of an unedited manuscript that has been accepted for publication. As a service to our customers we are providing this early version of the manuscript. The manuscript will undergo copyediting, typesetting, and review of the resulting proof before it is published in its final form. Please note that during the production process errors may be discovered which could affect the content, and all legal disclaimers that apply to the journal pertain.

Appendix A. Supplementary material

Supplementary material is provided and will be available online.

AUTHOR DECLARATION

We wish to draw the attention of the Editor to the following facts which may be considered as potential conflicts of interest and to significant financial contributions to this work.

Bryan Howell is a paid consultant for Abbott Laboratories. **Robert E. Gross** has research supported by Medtronic, PLC, Boston Scientific Corp., Neuropace, SanBio, Voyager Therapeutics and Abbott Laboratories; is a paid consultant for Medtronic, PLC, Voyager Therapeutics, SanBio, Zimmer Biomet and Abbott Laboratories; and is a shareholder in Nia Therapeutics. **Philip A. Starr** has research supported by Medtronic, PLC and Boston Scientific, Co. **Jon T. Willie** is a paid consultant for Medtronic, PLC and Neuropace, Inc. **Cameron C. McIntyre** is a paid consultant for Boston Scientific, Co., receives royalties from Hologram Consultants, Neuro Medical, and Qr8 Health, and is a shareholder in the following companies: Hologram Consultants, Surgical Information Sciences, CereGate, Autonomic Technologies, Cardionomic, Enspire DBS. **All other authors** have no competing interests.

We confirm that the manuscript has been read and approved by all named authors and that there are no other persons who satisfied the criteria for authorship but are not listed. We further confirm that the order of authors listed in the manuscript has been approved by all of us.

We confirm that we have given due consideration to the protection of intellectual property associated with this work and that there are no impediments to publication, including the timing of publication, with respect to intellectual property. In so doing we confirm that we have followed the regulations of our institutions concerning intellectual property.

We further confirm that any aspect of the work covered in this manuscript that has involved either experimental animals or human patients has been conducted with the ethical approval of all relevant bodies and that such approvals are acknowledged within the manuscript.

We understand that the Corresponding Author is the sole contact for the Editorial process (including Editorial Manager and direct communications with the office). She is responsible for communicating with the other authors about progress, submissions of revisions and final approval of proofs. We confirm that we have provided a current, correct email address which is accessible by the Corresponding Author and which has been configured to accept email from svjetlana.miocinovic@emory.edu.

Signed by all authors as follows:


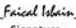







Abstract

Background: Subthalamic deep brain stimulation (DBS) is an effective surgical treatment for Parkinson's disease and continues to advance technologically with an enormous parameter space. As such, *in-silico* DBS modeling systems have become common tools for research and development, but their underlying methods have yet to be standardized and validated.

Objective: Evaluate the accuracy of patient-specific estimates of neural pathway activations in the subthalamic region against intracranial, cortical evoked potential (EP) recordings.

Methods: Pathway activations were modeled in eleven patients using the latest advances in connectomic modeling of subthalamic DBS, focusing on the hyperdirect pathway (HDP) and corticospinal/bulbar tract (CSBT) for their relevance in human research studies. Correlations between pathway activations and respective EP amplitudes were quantified.

Results: Good model performance required accurate lead localization and image fusions, as well as appropriate selection of fiber diameter in the biophysical model. While optimal model parameters varied across patients, good performance could be achieved using a global set of parameters that explained 60% and 73% of electrophysiologic activations of CSBT and HDP, respectively. Moreover, restricted models fit to only EP amplitudes of eight standard (monopolar and bipolar) electrode configurations were able to extrapolate variation in EP amplitudes across

<u>Bryan Howell</u> Print Name	 Signature	<u>10/15/2020</u> Date
<u>Faical Isbaine</u> Print Name	 Signature	<u>10/15/2020</u> Date
<u>Jon T. Willie</u> Print Name	 Signature	<u>10/15/2020</u> Date
<u>Enrico Opri</u> Print Name	 Signature	<u>10/15/2020</u> Date
<u>Robert E. Gross</u> Print Name	 Signature	<u>10/17/20</u> Date
<u>Coralie De Hemptinne</u> Print Name	 Signature	<u>10/15/2020</u> Date
<u>Phillip A. Starr</u> Print Name	 Signature	<u>10/15/20</u> Date
<u>Cameron C. McIntyre</u> Print Name	 Signature	<u>10/17/20</u> Date
<u>Svetlana Miodinovic</u> Print Name	 Signature	<u>10/15/2020</u> Date

other directional electrode configurations and stimulation parameters, with no significant reduction in model performance across the cohort.

Conclusions: Our findings demonstrate that connectomic models of DBS with sufficient anatomical and electrical details can predict recruitment dynamics of white matter. These results will help to define connectomic modeling standards for preoperative surgical targeting and postoperative patient programming applications.

Keywords

deep brain stimulation; subthalamic nucleus; Parkinson's disease; electrocorticography; evoked potentials; biophysical modeling

Introduction

Deep brain stimulation (DBS) is an effective adjunctive treatment for Parkinson's disease (PD) and other movement disorders [1], and continues to evolve technologically [2] with new applications [3]. When successful, the effects of DBS are dramatic, reducing symptoms in PD by 50% or more off medication [4]. However, DBS outcomes are variable due to heterogeneity in patient selection [5], electrode placement [6], and device programming [7]. It is infeasible to explore empirically the enormous parameter space of modern DBS systems [8], so *in-silico* models of DBS [9,10] are natural solutions to study advanced concepts before they proceed to clinical studies.

A recent trend in DBS research is the use of connectomic modeling [11]. This research sits at the intersection of brain connectomics and bioelectromagnetism, and is an evolving strategy that is driving innovation in both motor and psychiatric indications for DBS. Core to this concept is the tenet that DBS outcomes are influenced by the specific neuronal pathways activated by the extracellular stimulus [12–14]. These kinds of model-based analyses have provided useful insights for DBS, primarily in revealing *hot spots* of critical white matter activation not observable with neuroimaging alone [15,16]. As such, connectomic modeling is defining a new era of DBS research, with model-based strategies that rival [17] and, in some cases, outperform best clinical judgement [18,19]. However, caution remains in adopting model-based design for prospective DBS research due, primarily, to an absence of quality standards for their implementation [20].

Current standards for connectomic modeling are lacking, and models are typically assessed based on their capacity to estimate complex and temporally evolving clinical behaviors, which we find problematic for two reasons. First, it is premature to evaluate a model's merits when we are only beginning to pinpoint the specific pathway modulations that ameliorate PD symptoms [21–24]. And second, the degree of anatomical and electrical realism that is adequate for modeling axonal responses to DBS stimuli remains undetermined. For simplicity, many connectomic DBS research studies derive their connectomic estimates using volumetric algorithms of current spread, whose methodologies are varied and unvalidated [25–27], and suffer from issues of generalizability and accuracy [13,28]. Nonetheless, application of these unvalidated methods to clinical outcomes analyses has become common in DBS research [29] and, unfortunately, preceded any demonstration

of utility in generating prospective predictions with any degree of accuracy [30]. Extant gaps between accuracy and realism can be bridged by more modern connectomic frameworks that integrate scientifically rigorous biophysical principles and patient-specific brain anatomy [31–33], but there is still a need to assess first if these detailed *in silico* systems actually provide a reliable proxy for activation of known pathways.

An important next step in the field of connectomic DBS modeling is validation of its underlying methods and strategies. This study employs the latest advances in connectomic DBS modeling [34,35], with the objective of testing model predictions against electrophysiological biomarkers of pathway activation in the subthalamic region [36]. We use the hyperdirect pathway (HDP) and corticospinal/bulbar tract (CSBT) as testbeds, as we previously demonstrated that their degree of activation could be estimated using potentials recorded with electrocorticography (ECoG) during subthalamic DBS in PD patients [37,38]. While the HDP [22,23,39–41] and CSBT [42] are of considerable interest in subthalamic DBS, this study was not designed to ascertain which white matter pathways are critical to best therapeutic outcomes. That said, this study is the first to test rigorously connectomic modeling predictions against well-designed experimental measurements across varied patients, lead designs, and stimulation settings.

Materials and methods

Patient selection

Patients analyzed in this study were individuals with idiopathic Parkinson's disease scheduled to undergo STN DBS surgery at University of California San Francisco or Emory University. Informed consent was obtained before surgery under protocols approved by the Institutional Review Boards at both these universities. All patients were aware that the temporary subdural ECoG recording electrode was used strictly for research purposes. Evoked potential (EP) data has been previously published for Patients 1 and 7–11 [37]. Two patients whose DBS leads were repositioned for clinical reasons after EP recordings were excluded from our analyses.

Surgery and electrocorticography

A subdural ECoG recording electrode array (Ad-Tech) was placed on the surface of the brain through the same burr hole used for DBS implantation [43–45]. The 28-contact electrode array had two rows of fourteen, 2-mm diameter platinum contacts separated by 4 mm. The target location for the center of the array was the arm area of M1, 3 cm from the midline. Recordings were conducted at least 12 h after stopping anti-parkinsonian medications and at least 30 min after stopping propofol sedation. DBS electrodes were placed in the STN using microelectrode guidance. ECoG electrode location was determined using intraoperative CT registered to the preoperative MRI in surgical planning software (Framelink 5.1, Medtronic).

ECoG potentials were recorded using the Neuro Omega (Alpha Omega Engineering) or TDT PZ5 (Tucker Davis Technologies; Patients 9, 11) acquisition systems. An ipsilateral scalp needle (UCSF) or ear electrode (Emory) was used as a recording reference while the

corresponding contralateral electrode served as the ground. Signals were amplified and acquired at a 22 kHz sampling rate with a built-in hardware bandpass filter between 0.075 and 3500 Hz for Neuro Omega, and a 24,414 Hz sampling rate and 1–10,000 Hz bandpass filter for TDT.

DBS leads

Both standard (Medtronic 3387 and 3389, and Boston Scientific 2201) leads and current-steerable (Boston Scientific 2202 and Abbott Laboratory 6172) leads were implanted in patients. Lead 3387 has four cylindrical / ring contacts 1.5 mm in height, 0.635 mm in radius and spaced 1.5 mm apart from edge-to-edge. Lead 3389 is similar to 3387 except with 0.5 mm electrode spacings. Lead 2201 has eight contacts with the same geometry as 3389. Note, contact 0 is the most ventral (deepest) contact for Leads 3387 and 3389; otherwise, contact 1 is the most ventral contact. Lead 6172 has two outer ring contacts (1 and 4) and two sets of inner pseudo-ring contacts (2A/B/C and 3A/B/C). Segmented contacts for Lead 6172 are 104° arcs, equally spaced, and counted clockwise, with Contacts 2A and 3A pointing anterior and confirmed with intraoperative fluoroscopy. Lead 2202 has a similar design to 6172 but with some differences: the lead radius is 0.65 mm, the two sets of segmented contacts (2–4 and 5–7) are 90° arcs and counted counterclockwise, and contact 1 is a 0.85 mm height cylinder combined with the hemispherical cap. A detailed summary of lead geometries is found in [46].

Subthalamic DBS

Stimulation of the subthalamic region was conducted while patients were at rest using the NeuroOmega stimulator (Patients 1–6, 8, and 10), Medtronic digital stimulator (Model 8840; Patients 9, 11), or Medtronic analog stimulator (Model 3625; Patient 7). The NeuroOmega system used in eight patients was programmed to mimic the Medtronic clinical stimulators used in the remaining three patients [47,48]. Clinical DBS systems utilize asymmetric biphasic pulses consisting of a short “active” phase followed by a long, charge-balanced “recovery” phase. The NeuroOmega system was configured with the following instructions: the interphase delay was set to 70 μ s; and the recovery phase was set eight times lower in amplitude and eight times longer in duration than the active phase, with a maximum phase duration of 500 μ s allowable by the system. While clinical stimulators generally have a longer recharge phase (up to several milliseconds), the active phase primarily drives neural activation, so a longer recovery phase is expected to have minimal or no difference on activation thresholds [49].

Cathodes were denoted with a minus (–), anodes with a plus (+), and return electrodes for monopolar were a large surface electrode on the contralateral shoulder to emulate the stimulator case (C). Stimulation was primarily conducted at 10 Hz to ease the identification of the cortical evoked potentials, and because prior work showed that EP amplitudes at low frequencies were comparable to clinical high frequencies at 130 Hz [37]. Stimulation settings were tested for 10–15 s with a 3–5 s pause between the settings. The number of settings tested in each patient ranged from 18–45 and varied between patients depending on the amount of intraoperative time available. The order of stimulation settings was randomized in 8 of the 11 patients. Constant current stimulation was used whenever

available to control the amount of charge injected. In cases where voltage was regulated (Patients 7, 9, 11), the contact impedance was measured using a Medtronic digital stimulator (bipolar montage, 100 Hz), and the estimated applied current was calculated per Ohm's law using the average impedance of the DBS electrode before and after stimulation.

376 settings were tested across the cohort. Electrode configurations were either monopolar with one source /anode (9 settings) or sink /cathode (148 settings) on the lead, pseudo-monopolar with multiple contiguous anodes (2 settings) or cathodes (20 settings), or bipolar with an anode-cathode pair on the lead (197 settings). Pulse widths were primarily 60 μ s (356 settings), but also 30 μ s (10 settings) or 120 μ s (10 settings). Amplitudes were either 1 mA, 3 mA, or 5 mA; and frequencies were either 10 Hz (368 settings) or 130 Hz (8 settings). Omnidirectional settings referred to either ring electrodes in a monopolar configuration or co-activation of the three directional electrodes in a pseudo-ring configuration. For pseudo-ring configurations with all three segmented contact activated, the total applied current was divided evenly between the segments (e.g. for 5 mA, 1.33 mA was applied to each segment). Directional settings referred to any electrode configuration that directionally steered current around or along the lead axis; therefore, directional settings included bipolar ring configurations but excluded pseudo-ring configurations.

Evoked potentials

Raw ECoG potentials were re-referenced in a bipolar electrode configuration using adjacent contacts, aligned by stimulus start times, and averaged to generate EPs (from 100–150 pulses for each DBS setting). Peak latencies and peak amplitudes were visually determined for each stimulation setting. The EP amplitude was the voltage difference between a signal peak and its preceding trough, and the EP latency from the onset of the stimulus pulse was the time when the voltage peaked. Therefore, when present, EP₀ and EP₁ were distinct peaks: EP₀ indicated CSBT activation and had peak latency of approximately 1.5 ms, and EP₁ indicated HDP activation and had peak latencies of 2–4 ms [36,37]. Stimulation artifacts typically ended by 1 ms after the stimulus onset. In cases where EPs could not be separated from the large stimulation artifact, EP₀ and EP₁ were excluded from the analysis (2 DBS settings for Patient 7). Contact pairs overlying the precentral gyrus (M1) were used for analysis.

Activation of CSBT and HDP were quantified using EP₀ and EP₁, respectively. The concept of using short-latency cortical potentials to quantify antidromic activation of pathways with ECoG [50,51] or scalp EEG [52–54] is supported by prior DBS studies both in animals [55,56] and in humans [52–54]. Our previous experimental publication [37] demonstrated that CSBT activation 1) produces a shorter latency cortical EP compared to HDP due to the large diameter of pyramidal tract axons; 2) is associated with muscle activation; 3) is producible by both STN and pallidal stimulation, whereas HDP is only activated by STN DBS; and 4) has a different cortical topography from HDP activation because CSBT originates from primary motor cortex, while HDP's origin is more widespread. Additionally, detailed biophysical analyses support the idea of differentiating CSBT and HDP based on their respective latencies [36].

Neuroimaging

Preoperative T1-weighted (T1w) MRI scans were acquired with 1.5T or 3T scanners at slice thicknesses of 1–1.5 mm and in-plane resolutions of 0.89–1.35 mm. 1.5T scanners included the Philips Achieva or the Siemens Avanto, and 3T scanners included the Siemens Skyra or the Siemens Prisma. Postoperative T1w scans were scheduled the day after the DBS surgery and acquired with 1.5 T scanners, including Siemens Avanto, Siemens Espree, and GE Signa HDxt, with slices thicknesses of 1.—1.5 mm and in-plane resolutions of 0.5078–1.0156 mm. Reference spaces for each patient were their preoperative T1w images, except for two patients (9, 11), whose images were unavailable, so their postoperative T1w images were used instead. Intraoperative CT scans were acquired using the Medtronic O-Arm (Models O1 and O2) with a slice thickness of 0.833 mm and in-plane resolutions of 0.415–0.7754 mm. Postoperative CT scans were acquired using a GE Lightspeed VCT, GE Discovery CT750, or a Siemens Somatom go.Top with slice thicknesses of 0.6–1.25 mm and in-plane resolutions of 0.4609–0.5488 mm. Patient 10 did not have a postoperative T1w image, so their postoperative CT was used instead.

Neuroimages were processed using the FMRIB Software Library (FSL) [57]. T1w images were corrected for RF/B1 inhomogeneities using FMRIB's Automated Segmentation Tool, FAST [58], and skull-stripped using FSL's Brain Extraction Tool, BET [59]. CT images were thresholded (0–750), smoothed with a Gaussian kernel ($\sigma = 1$ mm), and skull-stripped using BET. Images were registered using FSL's image registration tool, FLIRT [60,61]. Intra-patient images were co-registered (cost function = Normalized Mutual Information) using a rigid body affine transformation unless registrations were poor, in which case, a twelve-parameter affine transformation was used instead (Patients 1, 3, 6). Brain masks were used to co-register CT and T1 spaces. The standard CIT 168 [62] brain atlas was registered to the patient's preoperative T1w space using FSL's nonlinear registration tool, FNIRT [63], and all registrations were visually confirmed for good quality.

Lead artifacts were localized in MATLAB (R2019a, Natick, MA) with thresholding and orthogonal distance regression (ODR). White lead artifacts in intraoperative CT images were demarcated using the brightest 5 % of image intensities, and a rigid lead trajectory was fit to these voxels using ODR. Dark lead artifacts in postoperative T1w images were demarcated in the same manner, except images were thresholded between absolute intensities of 0 and 500. In either case, the inferior end of the best fit line was considered the hemispherical lead tip, and contact centers were calculated based on their respective lead geometry.

Anatomical pathways

CSBT and HDP were modeled using an anatomical pathway atlas of the subthalamic region (Fig. 1) defined in the CIT168 space [35]. CSBT consisted of ten subdivisions based on the origins (termini) of corticofugal (corticopetal) projections defined in the atlas: that is, face and neck, upper extremities, and lower extremities of the primary motor cortex (M1, 1–3); the premotor cortex (4); the supplementary motor area (SMA, 5); the anterior cingulate cortex (ACC, 6); the dorsolateral and dorsomedial prefrontal cortices (dlPFC and dmPFC, 7–8); and the ventrolateral and ventromedial PFC (9–10). CSBT was consolidated in motor (1–5) and limbic (6–10) subdivisions. HDP was organized in the same manner as CSBT

without Subdivisions 7 and 8. The main trunk of HDP axons projecting from the cortex also contained a single collateral branch terminating in the STN with a fiber diameter 1/3 of that of their parent body [64]. Pathways were individualized by nonlinearly warping the data from CIT168 space to the patient's preoperative T1w space.

Biophysical modeling

Electric field models of DBS were built in COMSOL (v5.1). The volume conductors consisted of the DBS lead encapsulated within a uniform glial scar ($\sigma_{\text{scar}} = 0.1 \text{ S/m}$ [65], thickness = 0.5 mm) and surrounded by homogeneous brain tissue ($\sigma_{\text{brain}} = 0.2 \text{ S/m}$ [66], dimensions = 60 mm x 60 mm x 60 mm). DBS leads were modeled using internal boundary layers. Active (anodic and cathodic) sources were modeled with Dirichlet Boundary conditions: monopolar configurations (e.g., C+0-) were modeled using a non-zero voltage at one electrode and a zero voltage at the outer boundary of the model, representing a remote shoulder return electrode, and bipolar configurations were modeled using non-zero voltages of opposite polarity at two electrodes. Inactive contacts were modeled using a mixed boundary condition with two constraints per electrode: one, the equality of all surface electric potential, and two, no net current flow through the electrode surface. This floating potential boundary condition was used to model efficiently the effects of highly conductive passive electrodes on the millimeter scale. While heterogeneous dynamics of the electrode-tissue interface at the submillimeter scale produce a dispersion of time constants of voltage decay across the active contact, at the millimeter scale, the temporal dynamics of voltage decay are more spatially uniform [32,67] and thereby can be approximated with an equivalent one-dimensional circuit model [68]. Ideal insulators were modeled using homogeneous Neumann boundary conditions with zero current density (A/m^2). The tissue models for standard leads (3387, 3389, and 2201) were axially symmetric and thereby discretized in 2D using 4,021 third-order elements and 8,240 nodes. The tissue models for steerable leads (6172 and 2202) were discretized in 3D using 1,429,416 elements and 6,524,354 nodes. For efficiency, the patients' lead and axonal coordinates were rigidly transformed so that the lead was oriented along the positive z axis with its tip at the origin, preserving the discretization of the 2D and 3D tissue models across all patients.

Electric potentials (Φ) in the tissue medium at the onset of the stimulus pulse were numerically approximated by solving Laplace's equation,

$$\nabla \cdot (\Sigma \cdot \nabla \Phi) = 0$$

with the Finite Element Method (FEM), where Σ is tensor conductivity field. The temporal variation of Φ was approximated by multiplying the quasi-static solution of Laplace's equation with a waveform derived from an equivalent circuit model stimulation [32,68] with constant current-regulation.

Thresholds of direct axonal responses to extracellular stimulation were estimated using a predictive algorithm [34] based on the force driving polarization of the axonal membrane [69]. Briefly, locations of Nodes of Ranvier of axons within the CSBT and HDP were interpolated based on their fiber/body diameter [70] and spline-based trajectories. We used

the vector of extracellular potentials applied to each axon to calculate a modified driving force [71] based on the weighted integration of the most polarizing currents at the Nodes of Ranvier [72]. The driving force metric was then used to estimate stimulation thresholds for all axons in the CSBT and HDP. We examined the response of fiber diameters ranging from 4 μm to 20 μm [34].

Models of mammalian axons [70] and volume conduction for DBS [32,68,73] have been previously developed, so model parameters were chosen to be consistent with prior DBS modeling works, for consistency. Because white matter is composed of axons with a wide range of fiber diameters, modeling studies generally use a single representative fiber size to estimate a pathway's response to DBS in the absence of human histological data. Given that fiber diameter is often a free parameter in biophysical models of DBS, we focused on determining its value using EP amplitudes.

Statistical analyses

We evaluated responses to 376 stimulation settings (i.e., combinations of electrode configuration, pulse width, amplitude, and frequency) spanning eleven patients (Table 1) to test the hypotheses that EP_0 and EP_1 amplitudes vary in proportion to the percent activation of CSBT and HDP, respectively (Fig. 2). Model performance was quantified using the coefficient of determination (R^2) between the electrophysiologic EP amplitude and the respective pathway activation. EP_1 was never all zeros for any given patient. However, EP_0 was zero for all settings tested in Patients 7, 10, and 11; with no variance in EP_0 , R^2 was indeterminable. In these cases, we used a secondary metric of accuracy, defined as the percentage of correct assessments of true positives (activation) and negatives (no activation), to assess correspondence between the model predictions and the intraoperative measurements. Statistical comparisons between distributions of R^2 were conducted using a two-sample Kolmogorov-Smirnov test with $\alpha = 0.05$. We first evaluated the most important model variants to assess optimal performance and then used the best general set of global model parameters to explore potential sources of unexplained variability. Because our results focus on the biophysical aspects of model refinement and testing, we leave a more thorough analysis of lead localization in the Appendix A.

Model fidelity was further evaluated in each patient by evaluating the performance of a set of restricted models fit to only a subset of stimulation settings. We first determined if there was a consistent trend in which types of stimulation settings could reliably predict EP amplitudes of other settings across patients. We limited the initial search to sets of four stimulations settings, which is the minimal number of settings tested during a standard programming session in the clinic, and then we determined how many data points, at minimum, per patient were needed to extrapolate reliability all other data points not included in the regression fits.

Results

The study's objective was to evaluate model performance in estimating activation of CSBT and HDP (Figs. 1 and 2) against direct electrophysiological measurements of their activation

[37]. This work builds on a prior modeling study of subthalamic DBS [36], extending analyses to varied patients, lead designs, and stimulation settings (Table 1).

Optimal model performance

DBS leads were first localized using intraoperative CT images (Fig. A.1) acquired during the experiments. Average model performance was relatively poor ($R^2 < 0.5$), so leads were relocalized in the postoperative images using FSL's nonlinear registration algorithm with the same registration settings across all patients. Discrepancies in the lead's position differed by several millimeters between the localizations defined by intra-operative CT vs. post-operative T1w images for many patients (Fig. A.1A). With CT images, R^2 ranged from 0.25–0.67 (median = 0.46) for CSBT and from 0.09–0.92 (median = 0.49) for HDP, and when re-localizing leads with T1w images, model performance improved in 5/8 patients for CSBT and in 7/11 patients for HDP (Fig. A.1B), yielding a median R^2 of 0.60 and 0.73 for CSBT and HDP, respectively (Fig. A.1C). Therefore, the post-operative T1w images were used for all subsequent model analyses.

The actual distribution of fiber diameters within each pathway is unknown across patients. Therefore, the second optimization step looked at empirically selecting fiber diameters in the biophysical model that best represented the electrophysiological activations of CSBT and HDP for each patient. Model performance generally increased with increasing fiber diameter (Fig. 3A) with a relatively constant accuracy in predicting activation (true positive) versus no activation (true negative) (Fig. 3B). Across individuals, R^2 ranged from 0–0.83 for CSBT and from 0.16–0.92 for HDP. Although the optimal fiber diameter varied by patient, the trend of better accuracy with a larger fiber diameter was consistent across most subjects. Comparable model performance was achieved using a single fiber diameter of 12 μm for CSBT, and a single pair of fibers diameters for HDP of 12 μm and 4 μm for the corticofugal axon and collateral, respectively (Fig. 3C). Those representative fiber diameters were then used for all subsequent analyses.

The third optimization step assessed how anatomical organization of the pathways (Fig. 4A/C) affected subsequent model predictions. We predicted that nonmotor subdivisions of pathways would poorly predict variance in the evoked responses because ECoG data were acquired from electrodes overlying the primary motor cortex (M1) (Fig. 2A). As expected, activation of limbic subdivisions of pathways alone were poor predictors of EP_0 and EP_1 compared to motor subdivisions, but removing limbic subdivisions did not improve model performance (Fig. 4B/D). We found that model performance was optimal with a broader coverage of the internal capsule that included both motor and limbic fibers.

Sources of variance

We used the best representative model parameters across the cohort (i.e., postoperative T1w lead localizations, all anatomical subdivisions of the axonal pathways, and a single fiber diameter of 12 μm for the corticofugal axons) to evaluate potential sources of unexplained variance. Errors in estimating evoked responses (i.e., (predicted value – actual value) / actual value) had a discernable positive skew for directional bipolar and segmented cases compared to monopolar and ring cases, respectively (Fig. 5A). Therefore, we refitted models using

only data acquired with omnidirectional (monopolar, ring) electrodes and stimuli. Omitting directional stimulation cases improved model performance, particularly for patients with steerable leads: R^2 improved from 0.66 to 0.95 for Patient 4, from 0.66 to 0.77 for Patient 5, and from 0.48 to 0.73 for Patient 6 (Fig. 5B). Moreover, improvements in model performance were more pronounced for HDP than CSBT (Fig. 5C); median R^2 increased from 0.60 to 0.62 for CSBT and from 0.73 to 0.81 for HDP. As expected, EP_0 was the largest when the active contacts were in the posterolateral STN, closest to the CSBT (Fig. 6). This is consistent with the expected orientation of the steerable contacts, so errors were more likely to be a product of other factors, such as but not limited to heterogeneity in the anatomical distribution of pathways not captured by the pathway models (Fig. 6B).

Despite good model performance within each patient, aggregation of data across patients degraded the models' predictive power (Fig. 7). Degraded performance from aggregation (and normalization) could be explained as a product of two factors. First, an increase in unexplained variance from patients with the worst model performance (i.e., those with the lowest R^2). Second, an accumulation of unexplained inter-patient variability, meaning that the rate of change of EP amplitudes and their maximum values were variable functions of percent activation across patients. Therefore, patient-specificity was key to good model performance.

The four settings in each patient with the smallest errors were a combination of monopolar and bipolar (pseudo) ring configurations with a cathode spanning all four ring contacts. For these settings, the pulse widths were all 60 μ s, and the amplitudes were primarily 5 mA. Restricted models fit to only four monopolar ring electrode configurations (e.g., C+0-, C+1-, C+2-, and C+3-) or four bipolar ring configurations (e.g., 1+0-, 2+1-, 3+2-, and 2+3-) performed worse than the full model fit to all settings, yielding a median $R^2 < 0.5$ across patients for CSBT (Fig. 4A/B) and HDP (Fig. 4C/D). However, when combined, the EP amplitudes of these eight standard ring settings predicted the EP amplitudes of all other patient's settings with a median R^2 of 0.60 and 0.73 for CSBT and HDP, respectively, across the cohort. Note, for Patients 4–6, few pseudo bipolar ring settings were tested, so the eight settings were C+0-, C+1-, C+2-, and C+3- at 3 mA and 5 mA. And for Patients 7, 9–11, only bipolar electrode configurations were tested, so the eight settings were 1+0-, 2+1-, 3+2-, and 2+3- at 3 mA and 5 mA. Therefore, capturing variation in EP amplitudes across contacts may be sufficient to predict variation responses across other directional electrode configurations, stimulation amplitudes, and pulse widths.

Discussion

This is the first study to evaluate patient-specific estimates of neural pathway activations against intracranial electrophysiologic recordings of axonal responses to DBS. Overall, model accuracy was good, with performance being critically dependent on accurate lead localization, appropriate selection of pathway fiber size, as well as the DBS lead type and electrode contact configuration used to fit the model parameters. While the absolute best model parameters were patient-specific, trends across the cohort were consistent, and a general set of model parameters (i.e., postoperative T1w lead localizations, 12 μ m fiber diameters, and the use of all anatomical pathway subdivisions) provided a suitable

alternative, yielding median R^2 of 0.60 and 0.73 in estimating electrophysiologic activations of CSBT and HDP, respectively. Nonetheless, model fits were patient-specific, meaning that the rate of change of EP amplitudes and their maximum values varied as a function of percent activation across patients, highlighting the importance of patient-specificity for extrapolation. Overall, our findings demonstrate that connectomic models of DBS can predict recruitment dynamics of white matter pathways, but the accuracy of these predictions is highly dependent on accurate localization of the lead and targets, explicit representations of the target fiber's geometry, and accurate estimates of the applied DBS field. Models that ignore these details are unlikely to capture reliably recruitment dynamics across varied pathways and DBS settings.

Determinants of model performance

Details that are often ignored or assumed to be of negligible importance in patient-specific models of DBS were actually critical determinants of good model performance. In particular, our results counter three simplifying assumptions commonly used in other DBS modeling analyses. First, positional uncertainties in the electrode locations are not negligible and may be on the order of several millimeters (Fig. A.1A) despite visually overlapping image co-registrations. While the lowest image resolution sets an error floor, positional errors remain unbounded due to a number of latent factors, including lead movement or rotations [74], brain shift and deformations from surgery [75,76], and errors from multiple registrations, particularly across (CT and MRI) imaging modalities [77–79]. While nonlinear registrations between intracranial anatomy can mitigate potential positional errors, positional uncertainties, if not mitigated through post processing, can be millimeter-sized from the combination of surgical factors, image coregistrations, and the finite resolution of the imaging [80].

Second, a pathway's effective excitability to DBS is variable across different pathways and patients, and cannot be discerned from its anatomical organization alone. Histological [81,82] and neuroimaging [83–85] priors can inform an initial guess, but determining a pathway's excitability requires taking into account the differential excitability and topology of its axonal constituents [86]. The most straight-forward way of calibrating a pathway's excitability is adjusting the fiber diameter value, but the optimal value is not known *a priori* and thereby should be empirically determined for each pathway based on electrophysiological data (Fig. 3).

And third, the traditional tripartite organization of the STN (into a dorsolateral motor part, a ventromedial associative part, and a medial limbic part) [87] likely underrepresents the overlapping [88] and varied topological organization of HDP and CSBT across patients [89–91]. Limbic subdivisions of our pathways were the poorest predictors of potentials evoked in the motor cortex (Fig. 4B/D), but their exclusion unexpectedly degraded model accuracy. This suggests that in the absence of neuronal tract tracing, it's empirically advantageous to cast a wide net and make no definitive *a priori* determination of how fibers are topologically organized in the STN (Figs. 4 and 6).

We also found that accurate field modeling is key to model performance [13,28]. Homogeneous, isotropic field calculations are the most parsimonious way of implementing

electrical realism, and were able to achieve overall good model accuracy (median R^2 0.60), but performance was limited, particularly for directional stimuli (Fig. 5). While gross misorientation of the steerable lead is possible from torsion after fixation to the skull [92], leads were held by a microdrive during ECoG recordings, and fluoroscopy and EP measurements (Fig. 6B) were consistent with the desired lead orientation. Therefore, we posit that the relative underperformance of modeled directional cases compared to omnidirectional (monopolar, ring) were more a product of, and can be rectified by modeling inter-patient variability in the peri-electrode environment. This variability arises endogenously, from anisotropy and heterogeneity [32,93], and exogenously, from surgery, due to peri-electrode edema or air bubbles, loss of cerebrospinal fluid, and changes in intracranial pressure from pneumocephalus [94,95]. In other words, compared to omnidirectional settings that distribute current throughout the entire tissue medium, directional settings primarily guide current through local regions of tissue between contacts, and given this, the directional electric fields are more critically dependent on how readily current passes through these specific subregions. However, to what degree these electrical details should be incorporated is still an open question, and will likely depend on the target and use case for the model (e.g., pre-operative surgical targeting vs. post-operative parameter selection).

Implications for model-driven studies

The increasing complexity of DBS technologies provides an impetus for computational strategies to simplify and automate its clinical administration. DBS systems now provide segmented, cylindrical electrode arrays [46] that can interleave and/or couple multiple independent current sources [96], adding to an already enormous space of device stimulation parameters that cannot be explored within the limited time and resources available for clinical testing [97,98]. Providing physicians with an overwhelming amount of information – and options – is at odds with simplifying surgical planning and programming for DBS [7], so *in silico* systems are being employed to synthesize patients' data into actionable insights and instruction [99,100]. In addition, connectomic-based targeting is redefining surgical planning in psychiatric indications of DBS [18,19], but the merits of connectomic modeling for parameter selection for subthalamic DBS remain unclear [17,30,101].

DBS clinical outcomes are inextricably linked to underlying neural activations, specifically of myelinated axons [102–104]. Therefore, we postulate that optimizing models to predict accurately specific neural pathway activations is a necessary step for developing models that can predict DBS outcomes. Thus far, only volume of tissue activated (VTA) algorithms have been tested in clinical pilot studies, and those studies have generated inconsistent results [30,101] [13]. VTAs were originally designed as a coarse predictor, sacrificing accuracy for speed, to permit interactive visualizations of a very liberal upper bound on the potential spread of axonal activation [28], and thereby are significantly simplified compared to the biophysical models used in this study. VTAs may be useful for estimating a worst-case scenario of current spread, which has merit in avoiding unintended side effects [17]. However, VTAs ignore critical anatomical and electrical details that are essential for simulating neural responses [13]. As such, their utility for parameter titration based on pathway activations will likely be of limited assistance and prone to error [30]. The methods

[34,35] tested herein address the inherent methodological limitations of earlier approaches. New models that include more anatomical and electrical details, and correlate well with neural activation, should in theory also perform better at predicting DBS settings that provide therapeutic benefit. However, the actual clinical fidelity of these new types of DBS models awaits testing in a clinical trial.

We propose that standards are needed for the application of connectomic DBS modeling methods to clinical DBS studies, which begins with redefining the objectives. We recommend that connectomic models be evaluated based on well-defined electrophysiological measurements of neuronal activation [105–107]. Doing so distills concepts into testable hypotheses on which neural pathways are directly tied to symptom relief and/or disease state. This pivots the modeling strategy from predicting behavioral outcomes, which are idiosyncratic and temporally dynamic, to predicting direct physiological responses that are mechanistically well-defined [37,108,109]. Current trends in connectomic DBS research have focused on attempting to define correlations between coarsely modeled sites of activation and clinical behavioral measurements [29]. Unfortunately, application of these unvalidated model-based strategies have had limited assistance for clinical programming [30].

We also recommend that decisions based on modeled neural responses be patient-specific [20]. As demonstrated, inter-patient variability in neural responses were a confounding factor for model predictions when aggregated and normalized (Fig. 7). Therefore, the rate of change of EP amplitudes and their maximum values varied as a function of percent activation across patients, and is one potential reason why normative models have failed to predict accurately behavioral outcomes in individual patients [29,110–115]. Even within homogeneous cohorts of patients with PD, there is no globally best anatomical target, as best locations across patients span the entire STN and zona incerta [116,117]. This general finding implicates a number of candidate therapeutic white matter targets that can be activated from various lead positions. While this study was not designed to ascertain which of the subthalamic white matter pathways are critical to best therapeutic outcomes, our results highlight the importance of preserving inter-patient variance in attempts to understand neural responses to DBS.

Limitations

The models implemented herein simplified certain anatomical and electrical details. First, we ignored anisotropy and heterogeneity present within the brain [32] and soft tissues [33]. Solving highly detailed MRI-based head models for all pathways and stimulation settings requires days to complete for a single patient, even if parallelized on a compute cluster. These limitations prohibit high-throughput analysis of many patients and combinations of model parameters. Additionally, we estimated patients' pathways by nonlinearly mapping known anatomical connections derived from (human and non-human) primate histological results in a high-resolution brain atlas to the patients' MRI, [35], as opposed to tractography. While tractography has merit for studying inter-patient structural differences in white matter connectivity, this technique is computationally demanding, limited in its anatomical accuracy [118], and prone to errors from spurious connections and registration with low-

resolution scans [76,119]. Our goal was to capture the general anatomy of known pathways in the subthalamic region, and as such, the anatomical pathways atlas addressed some limitations of tractography [35]. Although more detailed models of axon morphology [23,90] and volume conduction [13] may further improve model accuracy, we focused on methods that are currently being used for DBS planning in clinical research [120]. These models sacrifice some details for accuracy but provide a consistent and tractable framework for high-throughput connectomic analyses.

Another limitation was that the putative associations between EP₀ and CSBT, and EP₁ and HDP in the primary motor cortex may not be exclusive, and some overlap in their latencies is expected. Smaller fibers in CSBT could contribute to EP₁, and initiation of action potentials in the corticofugal axon of HDP in the internal capsule could contribute to EP₀ [36]. However, given that EP₀ and EP₁ peaks were always distinct in our data [37], we did not add contributions of EP₀ to HDP or EP₁ to CSBT in the regression models due to the potential for overfitting.

Small sample size was another limitation and an inevitable challenge for invasive human recordings. We considered electrophysiologic recordings as the gold standard for defining HDP and CSBT activations. However, due to limited cortical coverage and variability in cortical electrode locations, it is likely that some relevant activations were missed. We took advantage of a repeated-measured design, testing over 350 settings across different patients and lead designs. Nonetheless, more studies are warranted to assess the consistency of our findings and determine what level of model accuracy is adequate for extrapolating model predictions, for different pathways and use cases.

Conclusions

Connectomic modeling of DBS is driving innovation for DBS indications, with associated *in silico* tools that help navigate and evaluate the enormous parameter space of new DBS technologies capable of steering, combining, and/or interleaving currents between contacts. Patient-specific connectomic modeling with adequate electrical and anatomical realism can rapidly simulate individualized axonal responses to subthalamic DBS, and these biophysical predictions can be reliable across different patients and lead designs, albeit with some unexplained variability. Through rigorous comparison with electrophysiology, we identified a set of potential generalized best practices for connectomic modeling of subthalamic DBS, highlighting potential failure points of current DBS models in estimating pathway activation and where improvements are likely needed to improve their overall accuracy. That said, this study sets the stage for prospective model-based design of optimal stimulation strategies for subthalamic DBS based on activation of specific white matter bundles.

Acknowledgements

This work was supported by grants from the National Institute of Neurological Disorders and Stroke (K23NS097576, R01NS105690, and R01NS069779) and the National Institute of Mental Health (R01MH102238) of the National Institutes of Health. The authors thank Angela Noecker for assistance with visualization of the connectomic model data. This work made use of the High-Performance Computing Resource in the Core Facility for Advanced Research Computing at Case Western Reserve University.

Declaration of interest

Bryan Howell is a paid consultant for Abbott Laboratories. **Robert E. Gross** is a paid consultant for Medtronic, PLC and Abbot Laboratories. **Philip A: Starr** has research supported by Medtronic, PLC and Boston Scientific, Co. **Jon T. Willie** is a paid consultant for Medtronic, PLC and Neuropace, Inc. **Cameron C. McIntyre** is a paid consultant for Boston Scientific, Co., receives royalties from Hologram Consultants, Neuros Medical, and Qr8 Health, and is a shareholder in the following companies: Hologram Consultants, Surgical Information Sciences, CereGate, Autonomic Technologies, Cardionomic, Enspire DBS. **All other authors** have no competing interests.

Appendix

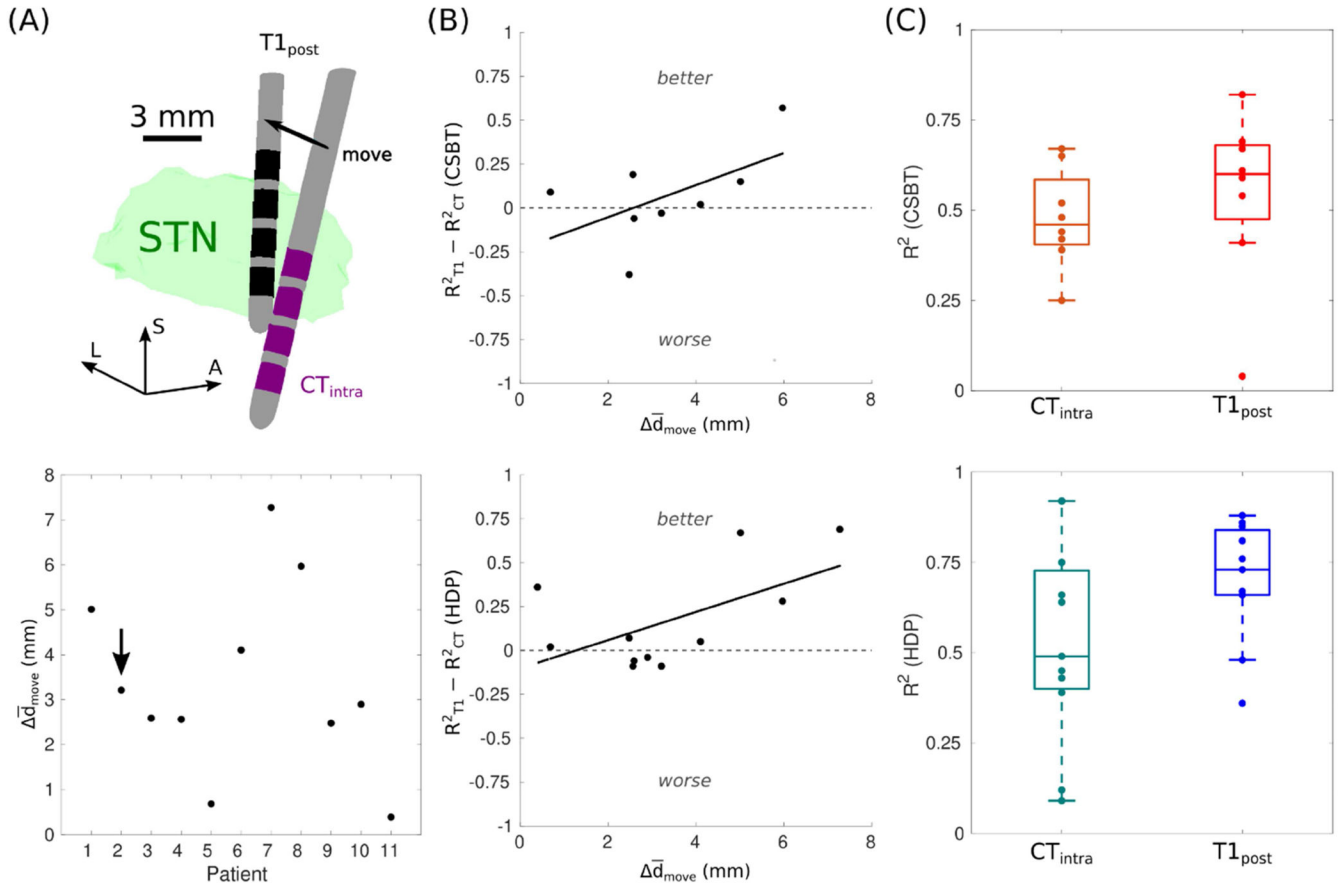


Figure A.1. Positional uncertainty was reduced with structural MRI lead localization.

(A) Average displacement between contact centers ($\Delta \bar{d}_{move}$) when the leads were localized with a postoperative T1-weighted (T1_{post}) image or an intraoperative CT (CT_{intra}) image. The black arrow points to Patient 2 depicted in the top panel. L = lateral, A = anterior, and S = superior. (B) The change in model performance compared to the magnitude of the positional shift when relocated with T1_{post}. R^2 = coefficient of determination, CSBT = corticospinal/bulbar tract, and HDP = hyperdirect pathway. (C) Model performance across the cohort with T1_{post} or CT_{intra}. R^2 were indeterminate for CSBT in Patient 7, 10, and 11 because EP_0 was zero for all their settings.

References

- [1]. Krack P, Volkmann J, Tinkhauser G, Deuschl G. Deep Brain Stimulation in Movement Disorders: From Experimental Surgery to Evidence-Based Therapy. *Movement Disorders* 2019;34:1795–810. 10.1002/mds.27860. [PubMed: 31580535]
- [2]. Ramirez-Zamora A, Giordano J, Gunduz A, Alcantara J, Cagle JN, Cernera S, et al. Proceedings of the Seventh Annual Deep Brain Stimulation Think Tank: Advances in Neurophysiology, Adaptive DBS, Virtual Reality, Neuroethics and Technology. *Frontiers in Human Neuroscience* 2020;14:54. 10.3389/fnhum.2020.00054. [PubMed: 32292333]
- [3]. Bina RW, Langevin J-P. Developing New Indications: Strategies and Hurdles to Discovery. In: Pouratian N, Sheth SA, editors. *Stereotactic and Functional Neurosurgery: Principles and Applications*, Cham: Springer International Publishing; 2020, p. 501–9. 10.1007/978-3-030-34906-6_35.
- [4]. Schuepbach WMM, Rau J, Knudsen K, Volkmann J, Krack P, Timmermann L, et al. Neurostimulation for Parkinson's Disease with Early Motor Complications. *N Engl J Med* 2013;368:610–22. 10.1056/NEJMoa1205158. [PubMed: 23406026]
- [5]. Bronstein JM, Tagliati M, Alterman RL, Lozano AM, Volkmann J, Stefani A, et al. Deep Brain Stimulation for Parkinson Disease: An Expert Consensus and Review of Key Issues. *Arch Neurol* 2011;68:165–. 10.1001/archneurol.2010.260. [PubMed: 20937936]
- [6]. Hamel W, Köppen JA, Alesch F, Antonini A, Barcia JA, Bergman H, et al. Targeting of the Subthalamic Nucleus for Deep Brain Stimulation: A Survey Among Parkinson Disease Specialists. *World Neurosurgery* 2017;99:41–6. 10.1016/j.wneu.2016.11.012. [PubMed: 27838430]
- [7]. Wagle Shukla A, Zeilman P, Fernandez H, Bajwa JA, Mehanna R. DBS Programming: An Evolving Approach for Patients with Parkinson's Disease. *Parkinson's Disease* 2017;2017:8492619. 10.1155/2017/8492619.
- [8]. Kuncel AM, Grill WM. Selection of stimulus parameters for deep brain stimulation. *Clinical Neurophysiology* 2004;115:2431–41. 10.1016/j.clinph.2004.05.031. [PubMed: 15465430]
- [9]. McIntyre CC, Foutz TJ. Computational modeling of deep brain stimulation. *Handb Clin Neurol* 2013;116:55–61. 10.1016/B978-0-444-53497-2.00005-X. [PubMed: 24112884]
- [10]. Capogrosso M, Lempka SF. A computational outlook on neurostimulation. *Bioelectronic Medicine* 2020;6:10. 10.1186/s42234-020-00047-3. [PubMed: 32490037]
- [11]. Wong JK, Middlebrooks EH, Grewal SS, Almeida L, Hess CW, Okun MS. A Comprehensive Review of Brain Connectomics and Imaging to Improve Deep Brain Stimulation Outcomes. *Movement Disorders* 2020;35:741–51. 10.1002/mds.28045. [PubMed: 32281147]
- [12]. McIntyre CC, Grill WM, Sherman DL, Thakor NV. Cellular effects of deep brain stimulation: model-based analysis of activation and inhibition. *J Neurophysiol* 2004;91:1457–69. 10.1152/jn.00989.2003. [PubMed: 14668299]
- [13]. Gunalan K, Howell B, McIntyre CC. Quantifying axonal responses in patient-specific models of subthalamic deep brain stimulation. *Neuroimage* 2018;172:263–77. 10.1016/j.neuroimage.2018.01.015. [PubMed: 29331449]
- [14]. Howell B, Choi KS, Gunalan K, Rajendra J, Mayberg HS, McIntyre CC. Quantifying the axonal pathways directly stimulated in therapeutic subcallosal cingulate deep brain stimulation. *Hum Brain Mapp* 2019;40:889–903. 10.1002/hbm.24419. [PubMed: 30311317]
- [15]. Butson CR, Cooper SE, Henderson JM, Wolgamuth B, McIntyre CC. Probabilistic analysis of activation volumes generated during deep brain stimulation. *NeuroImage* 2011;54:2096–104. 10.1016/j.neuroimage.2010.10.059. [PubMed: 20974269]
- [16]. Riva-Posse P, Choi KS, Holtzheimer PE, McIntyre CC, Gross RE, Chaturvedi A, et al. Defining Critical White Matter Pathways Mediating Successful Subcallosal Cingulate Deep Brain Stimulation for Treatment-Resistant Depression. *Biological Psychiatry* 2014;76:963–9. 10.1016/j.biopsych.2014.03.029. [PubMed: 24832866]
- [17]. Frankemolle AMM, Wu J, Noecker AM, Voelcker-Rehage C, Ho JC, Vitek JL, et al. Reversing cognitive–motor impairments in Parkinson's disease patients using a computational modelling

- approach to deep brain stimulation programming. *Brain* 2010; 133:746–61. 10.1093/brain/awp315. [PubMed: 20061324]
- [18]. Coenen VA, Sajonz B, Reisert M, Bostroem J, Bewernick B, Urbach H, et al. Tractography-assisted deep brain stimulation of the superolateral branch of the medial forebrain bundle (slMFB DBS) in major depression. *NeuroImage: Clinical* 2018;20:580–93. 10.1016/j.nicl.2018.08.020. [PubMed: 30186762]
- [19]. Riva-Posse P, Choi KS, Holtzheimer PE, Crowell AL, Garlow SJ, Rajendra JK, et al. A connectomic approach for subcallosal cingulate deep brain stimulation surgery: prospective targeting in treatment-resistant depression. *Mol Psychiatry* 2018;23:843–9. 10.1038/mp.2017.59. [PubMed: 28397839]
- [20]. Coenen VA, Schlaepfer TE, Varkuti B, Schuurman PR, Reinacher PC, Voges J, et al. Surgical decision making for deep brain stimulation should not be based on aggregated normative data mining. *Brain Stimulation: Basic, Translational, and Clinical Research in Neuromodulation* 2019;12:1345–8. 10.1016/j.brs.2019.07.014.
- [21]. Johnson MD, Miocinovic S, McIntyre CC, Vitek JL. Mechanisms and targets of deep brain stimulation in movement disorders. *Neurotherapeutics* 2008;5:294–308. 10.1016/j.nurt.2008.01.010. [PubMed: 18394571]
- [22]. Gradinaru V, Mogri M, Thompson KR, Henderson JM, Deisseroth K. Optical Deconstruction of Parkinsonian Neural Circuitry. *Science* 2009;324:354–9. 10.1126/science.1167093. [PubMed: 19299587]
- [23]. Anderson RW, Farokhniaee A, Gunalan K, Howell B, McIntyre CC. Action potential initiation, propagation, and cortical invasion in the hyperdirect pathway during subthalamic deep brain stimulation. *Brain Stimulation* 2018;11:1140–50. [PubMed: 29779963]
- [24]. Yu C, Cassar IR, Sambangi J, Grill WM. Frequency-Specific Optogenetic Deep Brain Stimulation of Subthalamic Nucleus Improves Parkinsonian Motor Behaviors. *J Neurosci* 2020;40:4323. 10.1523/JNEUROSCI.3071-19.2020. [PubMed: 32312888]
- [25]. Mädler B, Coenen VA. Explaining clinical effects of deep brain stimulation through simplified target-specific modeling of the volume of activated tissue. *AJNR Am J Neuroradiol* 2012;33:1072–80. 10.3174/ajnr.A2906. [PubMed: 22300931]
- [26]. Chaturvedi A, Luján JL, McIntyre CC. Artificial neural network based characterization of the volume of tissue activated during deep brain stimulation. *J Neural Eng* 2013;10:056023. 10.1088/1741-2560/10/5/056023. [PubMed: 24060691]
- [27]. Astrom M, Diczfalusy E, Martens H, Wardell K. Relationship between neural activation and electric field distribution during deep brain stimulation. *IEEE Trans Biomed Eng* 2015;62:664–72. 10.1109/TBME.2014.2363494. [PubMed: 25350910]
- [28]. Duffley G, Anderson DN, Vorwerk J, Dorval AD, Butson CR. Evaluation of methodologies for computing the deep brain stimulation volume of tissue activated. *Journal of Neural Engineering* 2019;16:066024. 10.1088/1741-2552/ab3c95. [PubMed: 31426036]
- [29]. Horn A, Reich M, Vorwerk J, Li N, Wenzel G, Fang Q, et al. Connectivity Predicts deep brain stimulation outcome in Parkinson disease. *Ann Neurol* 2017;82:67–78. 10.1002/ana.24974. [PubMed: 28586141]
- [30]. Béreau M, Kibleur A, Bouthour W, Tomkova Chaoui E, Maling N, Nguyen TAK, et al. Modeling of Electric Fields in Individual Imaging Atlas for Capsular Threshold Prediction of Deep Brain Stimulation in Parkinson's Disease: A Pilot Study. *Frontiers in Neurology* 2020;11:532. 10.3389/fneur.2020.00532. [PubMed: 32714264]
- [31]. Chaturvedi A, Butson CR, Lempka SF, Cooper SE, McIntyre CC. Patient-specific models of deep brain stimulation: influence of field model complexity on neural activation predictions. *Brain Stimulation* 2010;3:65–7. 10.1016/j.brs.2010.01.003. [PubMed: 20607090]
- [32]. Howell B, McIntyre CC. Analyzing the tradeoff between electrical complexity and accuracy in patient-specific computational models of deep brain stimulation. *J Neural Eng* 2016;13:036023. 10.1088/1741-2560/13/3/036023. [PubMed: 27172137]
- [33]. Howell B, McIntyre CC. Role of Soft-Tissue Heterogeneity in Computational Models of Deep Brain Stimulation. *Brain Stimul* 2017;10:46–50. 10.1016/j.brs.2016.09.001. [PubMed: 27720186]

- [34]. Howell B, Gunalan K, McIntyre CC. A Driving-Force Predictor for Estimating Pathway Activation in Patients-Specific Models of Deep Brain Stimulation. *Neuromodulation: Technology at the Neural Interface* 2019;22:403–15.
- [35]. Petersen MV, Mlakar J, Haber SN, Parent M, Smith Y, Strick PL, et al. Holographic Reconstruction of Axonal Pathways in the Human Brain. *Neuron* 2019;104:1056–1064.e3. 10.1016/j.neuron.2019.09.030. [PubMed: 31708306]
- [36]. Gunalan K, McIntyre CC. Biophysical reconstruction of the signal conduction underlying short-latency cortical evoked potentials generated by subthalamic deep brain stimulation. *Clinical Neurophysiology* 2020;131:542–7. 10.1016/j.clinph.2019.09.020. [PubMed: 31757636]
- [37]. Miocinovic S, de Hemptinne C, Chen W, Isbaine F, Willie JT, Ostrem JL, et al. Cortical Potentials Evoked by Subthalamic Stimulation Demonstrate a Short Latency Hyperdirect Pathway in Humans. *J Neurosci* 2018;38:9129. 10.1523/JNEUROSCI.1327-18.2018. [PubMed: 30201770]
- [38]. Chen W, de Hemptinne C, Miller AM, Leibbrand M, Little SJ, Lim DA, et al. Prefrontal-Subthalamic Hyperdirect Pathway Modulates Movement Inhibition in Humans. *Neuron* 2020;106:579–588.e3. 10.1016/j.neuron.2020.02.012. [PubMed: 32155442]
- [39]. Dejean C, Hyland B, Arbuthnott G. Cortical effects of subthalamic stimulation correlate with behavioral recovery from dopamine antagonist induced akinesia. *Cerebral Cortex* 2009;19:1055–63. [PubMed: 18787234]
- [40]. Li Q, Ke Y, Chan DC, Qian Z-M, Yung KK, Ko H, et al. Therapeutic deep brain stimulation in Parkinsonian rats directly influences motor cortex. *Neuron* 2012;76:1030–41. [PubMed: 23217750]
- [41]. Sanders TH, Jaeger D. Optogenetic stimulation of cortico-subthalamic projections is sufficient to ameliorate bradykinesia in 6-ohda lesioned mice. *Neurobiology of Disease* 2016;95:225–37. 10.1016/j.nbd.2016.07.021. [PubMed: 27452483]
- [42]. Tommasi G, Krack P, Fraix V, Le Bas J-F, Chabardes S, Benabid A-L, et al. Pyramidal tract side effects induced by deep brain stimulation of the subthalamic nucleus. *Journal of Neurology, Neurosurgery & Psychiatry* 2008;79:813–9. 10.1136/jnnp.2007.117507.
- [43]. Crowell AL, Ryapolova-Webb ES, Ostrem JL, Galifianakis NB, Shimamoto S, Lim DA, et al. Oscillations in sensorimotor cortex in movement disorders: an electrocorticography study. *Brain* 2012;135:615–30. [PubMed: 22252995]
- [44]. De Hemptinne C, Swann NC, Ostrem JL, Ryapolova-Webb ES, San Luciano M, Galifianakis NB, et al. Therapeutic deep brain stimulation reduces cortical phase-amplitude coupling in Parkinson's disease. *Nature Neuroscience* 2015;18:779–86. [PubMed: 25867121]
- [45]. Panov F, Levin E, de Hemptinne C, Swann NC, Qasim S, Miocinovic S, et al. Intraoperative electrocorticography for physiological research in movement disorders: principles and experience in 200 cases. *Journal of Neurosurgery* 2017;126:122–31. [PubMed: 26918474]
- [46]. Anderson DN, Osting B, Vorwerk J, Dorval AD, Butson CR. Optimized programming algorithm for cylindrical and directional deep brain stimulation electrodes. *J Neural Eng* 2018; 15:026005. 10.1088/1741-2552/aaa14b. [PubMed: 29235446]
- [47]. Trottenberg T, Winter C, Alesch F, Kupsch A. Risk of tissue damage and deep brain stimulation with external devices: A technical note. *Annals of Neurology* 2004;56:310–1. 10.1002/ana.20181. [PubMed: 15293292]
- [48]. Butson CR, McIntyre CC. Differences among implanted pulse generator waveforms cause variations in the neural response to deep brain stimulation. *Clinical Neurophysiology* 2007;118:1889–94. 10.1016/j.clinph.2007.05.061. [PubMed: 17581776]
- [49]. Foutz TJ, McIntyre CC. Evaluation of novel stimulus waveforms for deep brain stimulation. *Journal of Neural Engineering* 2010;7:066008. [PubMed: 21084732]
- [50]. Kelley R, Flouty O, Emmons EB, Kim Y, Kingyon J, Wessel JR, et al. A human prefrontal-subthalamic circuit for cognitive control. *Brain* 2018;141:205–16. 10.1093/brain/awx300. [PubMed: 29190362]
- [51]. Chen K-HS, Chen R. Invasive and Noninvasive Brain Stimulation in Parkinson's Disease: Clinical Effects and Future Perspectives. *Clinical Pharmacology & Therapeutics* 2019;106:763–75. 10.1002/cpt.1542. [PubMed: 31179534]

- [52]. Ashby P, Paradiso G, Saint-Cyr JA, Chen R, Lang AE, Lozano AM. Potentials recorded at the scalp by stimulation near the human subthalamic nucleus. *Clinical Neurophysiology* 2001;112:431–7. 10.1016/S1388-2457(00)00532-0. [PubMed: 11222963]
- [53]. Kuriakose R, Saha U, Castillo G, Udupa K, Ni Z, Gunraj C, et al. The Nature and Time Course of Cortical Activation Following Subthalamic Stimulation in Parkinson's Disease. *Cerebral Cortex* 2010;20:1926–36. 10.1093/cercor/bhp269. [PubMed: 20019146]
- [54]. Walker HC, Huang H, Gonzalez CL, Bryant JE, Killen J, Cutter GR, et al. Short latency activation of cortex during clinically effective subthalamic deep brain stimulation for Parkinson's disease. *Movement Disorders* 2012;27:864–73. 10.1002/mds.25025. [PubMed: 22648508]
- [55]. Li S, Arbutnott GW, Jutras MJ, Goldberg JA, Jaeger D. Resonant Antidromic Cortical Circuit Activation as a Consequence of High-Frequency Subthalamic Deep-Brain Stimulation. *Journal of Neurophysiology* 2007;98:3525–37. 10.1152/jn.00808.2007. [PubMed: 17928554]
- [56]. Kumaravelu K, Oza CS, Behrend CE, Grill WM. Model-based deconstruction of cortical evoked potentials generated by subthalamic nucleus deep brain stimulation. *Journal of Neurophysiology* 2018;120:662–80. 10.1152/jn.00862.2017. [PubMed: 29694280]
- [57]. Smith SM, Jenkinson M, Woolrich MW, Beckmann CF, Behrens TEJ, Johansen-Berg H, et al. Advances in functional and structural MR image analysis and implementation as FSL. *Neuroimage* 2004;23 Suppl 1:S208–219. 10.1016/j.neuroimage.2004.07.051. [PubMed: 15501092]
- [58]. Zhang Y, Brady M, Smith S. Segmentation of brain MR images through a hidden Markov random field model and the expectation-maximization algorithm. *Medical Imaging, IEEE Transactions On* 2001;20:45–57. 10.1109/42.906424.
- [59]. Jenkinson M, Pechaud M, Smith S. BET2: MR-based estimation of brain, skull and scalp surfaces. Eleventh annual meeting of the organization for human brain mapping, vol. 17, Toronto.; 2005, p. 167.
- [60]. Jenkinson M, Smith S. A global optimisation method for robust affine registration of brain images. *Med Image Anal* 2001;5:143–56. [PubMed: 11516708]
- [61]. Jenkinson M, Bannister P, Brady M, Smith S. Improved optimization for the robust and accurate linear registration and motion correction of brain images. *Neuroimage* 2002;17:825–41. [PubMed: 12377157]
- [62]. Pauli WM, Nili AN, Tyszka JM. A high-resolution probabilistic in vivo atlas of human subcortical brain nuclei. *Scientific Data* 2018;5:180063. 10.1038/sdata.2018.63. [PubMed: 29664465]
- [63]. Anderson JLR, Jenkinson M, Smith S. Non-linear registration, aka spatial normalisation. <http://www.fmrib.ox.ac.uk/datasets/techrep/>: 2010
- [64]. Gunalan K, Chaturvedi A, Howell B, Duchin Y, Lempka SF, Patriat R, et al. Creating and parameterizing patient-specific deep brain stimulation pathway-activation models using the hyperdirect pathway as an example. *PLoS ONE* 2017;12:e0176132. 10.1371/journal.pone.0176132. [PubMed: 28441410]
- [65]. Grill WM, Mortimer JT. Electrical properties of implant encapsulation tissue. *Annals of Biomedical Engineering* 1994;22:23–33. [PubMed: 8060024]
- [66]. Gabriel C, Peyman A, Grant EH. Electrical conductivity of tissue at frequencies below 1 MHz. *Phys Med Biol* 2009;54:4863–78. 10.1088/0031-9155/54/16/002. [PubMed: 19636081]
- [67]. Howell B, Naik S, Grill WM. Influences of interpolation error, electrode geometry, and the electrode-tissue interface on models of electric fields produced by deep brain stimulation. *IEEE Transactions on Biomedical Engineering* 2014;61:297–307. 10.1109/tbme.2013.2292025. [PubMed: 24448594]
- [68]. Lempka SF, Howell B, Gunalan K, Machado AG, McIntyre CC. Characterization of the stimulus waveforms generated by implantable pulse generators for deep brain stimulation. *Clin Neurophysiol* 2018;129:731–42. 10.1016/j.clinph.2018.01.015. [PubMed: 29448149]
- [69]. Rattay F Analysis of models for external stimulation of axons. *IEEE Transactions on Biomedical Engineering* 1986;33:974–7. 10.1109/tbme.1986.325670. [PubMed: 3770787]

- [70]. McIntyre CC, Richardson AG, Grill WM. Modeling the excitability of mammalian nerve fibers: influence of afterpotentials on the recovery cycle. *Journal of Neurophysiology* 2002;87:995–1006. [PubMed: 11826063]
- [71]. Peterson EJ, Izad O, Tyler DJ. Predicting myelinated axon activation using spatial characteristics of the extracellular field. *J Neural Eng* 2011;8:046030. 10.1088/1741-2560/8/4/046030. [PubMed: 21750371]
- [72]. Warman EN, Grill WM, Durand D. Modeling the effects of electric fields on nerve fibers: Determination of excitation thresholds. *IEEE Transactions on Biomedical Engineering* 1992;39:1244–54. 10.1109/10.184700. [PubMed: 1487287]
- [73]. Miciocinovic S, Lempka SF, Russo GS, Maks CB, Butson CR, Sakaie KE, et al. Experimental and theoretical characterization of the voltage distribution generated by deep brain stimulation. *Exp Neurol* 2009;216:166–76. 10.1016/j.expneurol.2008.11.024. [PubMed: 19118551]
- [74]. Schüpbach WMM, Chabardes S, Matthies C, Pollo C, Steigerwald F, Timmermann L, et al. Directional leads for deep brain stimulation: Opportunities and challenges. *Movement Disorders* 2017;32:1371–5. 10.1002/mds.27096. [PubMed: 28843016]
- [75]. Maier-Hein KH, Neher PF, Houde J-C, Côté M-A, Garyfallidis E, Zhong J, et al. The challenge of mapping the human connectome based on diffusion tractography. *Nature Communications* 2017;8:1349. 10.1038/s41467-017-01285-x.
- [76]. Choi KS, Noecker AM, Riva-Posse P, Rajendra JK, Gross RE, Mayberg HS, et al. Impact of brain shift on subcallosal cingulate deep brain stimulation. *Brain Stimulation* 2018;11:445–53. [PubMed: 29246748]
- [77]. Watanabe Y, Han E. Image registration accuracy of GammaPlan: a phantom study. *Journal of Neurosurgery* 2008;109:21–4. [PubMed: 19123884]
- [78]. Chung H-T, Kim JH, Kim JW, Paek SH, Kim DG, Chun KJ, et al. Assessment of image co-registration accuracy for frameless gamma knife surgery. *PLOS ONE* 2018;13:e0193809. 10.1371/journal.pone.0193809. [PubMed: 29499061]
- [79]. Burke JF, Tanzillo D, Starr PA, Lim DA, Larson PS. CT and MRI Image Fusion Error: An Analysis of Co-Registration Error Using Commercially Available Deep Brain Stimulation Surgical Planning Software. *Stereotactic and Functional Neurosurgery* 2021. 10.1159/000511114.
- [80]. Athawale TM, Johnson KA, Butson CR, Johnson CR. A statistical framework for quantification and visualisation of positional uncertainty in deep brain stimulation electrodes. *Computer Methods in Biomechanics and Biomedical Engineering: Imaging & Visualization* 2018.
- [81]. Aboitiz F, Scheibel AB, Fisher RS, Zaidel E. Fiber composition of the human corpus callosum. *Brain Res* 1992;598:143–53. [PubMed: 1486477]
- [82]. Liewald D, Miller R, Logothetis N, Wagner H-J, Schüz A. Distribution of axon diameters in cortical white matter: an electron-microscopic study on three human brains and a macaque. *Biol Cybern* 2014;108:541–57. 10.1007/s00422-014-0626-2. [PubMed: 25142940]
- [83]. Mohammadi S, Carey D, Dick F, Diedrichsen J, Sereno MI, Reisert M, et al. Whole-brain in-vivo measurements of the axonal g-ratio in a group of 37 healthy volunteers. *Frontiers in Neuroscience* 2015;9:441. [PubMed: 26640427]
- [84]. Axer M, Strohmer S, Gräbel D, Bücken O, Dohmen M, Reckfort J, et al. Estimating Fiber Orientation Distribution Functions in 3D-Polarized Light Imaging. *Frontiers in Neuroanatomy* 2016;10:40. 10.3389/fnana.2016.00040. [PubMed: 27147981]
- [85]. Veraart J, Nunes D, Rudrapatna U, Fieremans E, Jones DK, Novikov DS, et al. Noninvasive quantification of axon radii using diffusion MRI. *ELife* 2020;9:e49855. 10.7554/eLife.49855. [PubMed: 32048987]
- [86]. Tomasi S, Caminiti R, Innocenti GM. Areal differences in diameter and length of corticofugal projections. *Cerebral Cortex* 2012;22:1463–72. [PubMed: 22302056]
- [87]. Hamani C, Florence G, Heinsen H, Plantinga BR, Temel Y, Uludag K, et al. Subthalamic Nucleus Deep Brain Stimulation: Basic Concepts and Novel Perspectives. *ENeuro* 2017;4:ENEURO.0140-17.2017. 10.1523/ENEURO.0140-17.2017.

- [88]. Alkemade A, Schnitzler A, Forstmann BU. Topographic organization of the human and non-human primate subthalamic nucleus. *Brain Structure and Function* 2015;220:3075–86. 10.1007/s00429-015-1047-2. [PubMed: 25921975]
- [89]. Keuken M, Uylings H, Geyer S, Schäfer A, Turner R, Forstmann B. Are there three subdivisions in the primate subthalamic nucleus? *Frontiers in Neuroanatomy* 2012;6:14. 10.3389/fnana.2012.00014. [PubMed: 22590455]
- [90]. Coudé D, Parent A, Parent M. Single-axon tracing of the corticosubthalamic hyperdirect pathway in primates. *Brain Structure and Function* 2018;223:3959–73. 10.1007/s00429-018-1726-x. [PubMed: 30109491]
- [91]. van Wijk BCM, Alkemade A, Forstmann BU. Functional segregation and integration within the human subthalamic nucleus from a micro- and meso-level perspective. *Cortex* 2020;131:103–13. 10.1016/j.cortex.2020.07.004. [PubMed: 32823130]
- [92]. Lange F, Steigerwald F, Engel D, Malzacher T, Neun T, Fricke P, et al. Longitudinal Assessment of Rotation Angles after Implantation of Directional Deep Brain Stimulation Leads. *Stereotactic and Functional Neurosurgery* 2020. 10.1159/000511202.
- [93]. Schmidt C, van Rienen U. Modeling the field distribution in deep brain stimulation: the influence of anisotropy of brain tissue. *IEEE Transactions on Biomedical Engineering* 2012;59:1583–92. [PubMed: 22410323]
- [94]. Obuchi T, Katayama Y, Kobayashi K, Oshima H, Fukaya C, Yamamoto T. Direction and predictive factors for the shift of brain structure during deep brain stimulation electrode implantation for advanced Parkinson's disease. *Neuromodulation: Technology at the Neural Interface* 2008;11:302–10.
- [95]. Borellini L, Ardolino G, Carrabba G, Locatelli M, Rampini P, Sbaraini S, et al. Peri-lead edema after deep brain stimulation surgery for Parkinson's disease: a prospective magnetic resonance imaging study. *European Journal of Neurology* 2019;26:533–9. [PubMed: 30358915]
- [96]. Zhang S, Silburn P, Pouratian N, Cheeran B, Venkatesan L, Kent A, et al. Comparing current steering technologies for directional deep brain stimulation using a computational model that incorporates heterogeneous tissue properties. *Neuromodulation: Technology at the Neural Interface* 2020;23:469–77.
- [97]. Hunka K, Suchowersky O, Wood S, Derwent L, Kiss ZH. NursingTime to Program and Assess Deep Brain. *Journal of Neuroscience Nursing* 2005;37:205.
- [98]. Ondo WG, Bronte-Stewart H. The North American Survey of Placement and Adjustment Strategies for Deep Brain Stimulation. *Stereotactic and Functional Neurosurgery* 2005;83:142–7. [PubMed: 16205106]
- [99]. Noecker AM, Choi KS, Riva-Posse P, Gross RE, Mayberg HS, McIntyre CC. StimVision Software: Examples and Applications in Subcallosal Cingulate Deep Brain Stimulation for Depression. *Neuromodulation* 2018;21:191–6. 10.1111/ner.12625. [PubMed: 28653482]
- [100]. Horn A, Li N, Dembek TA, Kappel A, Boulay C, Ewert S, et al. Lead-DBS v2: Towards a comprehensive pipeline for deep brain stimulation imaging. *Neuroimage* 2019;184:293–316. 10.1016/j.neuroimage.2018.08.068. [PubMed: 30179717]
- [101]. Pourfar MH, Mogilner AY, Farris S, Giroux M, Gillego M, Zhao Y, et al. Model-Based Deep Brain Stimulation Programming for Parkinson's Disease: The GUIDE Pilot Study. *Stereotactic and Functional Neurosurgery* 2015;93:231–9. [PubMed: 25998447]
- [102]. Nowak LG, Bullier J. Axons, but not cell bodies, are activated by electrical stimulation in cortical gray matterI. Evidence from chronaxie measurements. *Experimental Brain Research* 1998;118:477–88. 10.1007/s002210050304. [PubMed: 9504843]
- [103]. Nowak LG, Bullier J. Axons, but not cell bodies, are activated by electrical stimulation in cortical gray matterII. Evidence from selective inactivation of cell bodies and axon initial segments. *Experimental Brain Research* 1998;118:489–500. 10.1007/s002210050305. [PubMed: 9504844]
- [104]. Holsheimer J, Demeulemeester H, Nuttin B, De Sutter P. Identification of the target neuronal elements in electrical deep brain stimulation. *European Journal of Neuroscience* 2000;12:4573–7. 10.1111/j.1460-9568.2000.01306.x.

- [105]. Devergnas A, Wichmann T. Cortical Potentials Evoked by Deep Brain Stimulation in the Subthalamic Area. *Frontiers in Systems Neuroscience* 2011;5:30. 10.3389/fnsys.2011.00030. [PubMed: 21625611]
- [106]. Kent AR, Swan BD, Brocker DT, Turner DA, Gross RE, Grill WM. Measurement of evoked potentials during thalamic deep brain stimulation. *Brain Stimul* 2015;8:42–56. 10.1016/j.brs.2014.09.017. [PubMed: 25457213]
- [107]. Irwin ZT, Awad MZ, Gonzalez CL, Nakhmani A, Bentley JN, Moore TA, et al. Latency of subthalamic nucleus deep brain stimulation-evoked cortical activity as a potential biomarker for postoperative motor side effects. *Clinical Neurophysiology* 2020;131:1221–9. 10.1016/j.clinph.2020.02.021. [PubMed: 32299006]
- [108]. Bhanpuri NH, Bertucco M, Ferman D, Young SJ, Liker MA, Krieger MD, et al. Deep brain stimulation evoked potentials may relate to clinical benefit in childhood dystonia. *Brain Stimul* 2014;7:718–26. 10.1016/j.brs.2014.06.003. [PubMed: 25088460]
- [109]. Waters AC, Veerakumar A, Choi KS, Howell B, Tiruvadi V, Bijanki KR, et al. Test-retest reliability of a stimulation-locked evoked response to deep brain stimulation in subcallosal cingulate for treatment resistant depression. *Hum Brain Mapp* 2018;39:4844–56. 10.1002/hbm.24327. [PubMed: 30120851]
- [110]. Calabrese E, Hickey P, Hulette C, Zhang J, Parente B, Lad SP, et al. Postmortem diffusion MRI of the human brainstem and thalamus for deep brain stimulator electrode localization. *Human Brain Mapping* 2015;36:3167–78. 10.1002/hbm.22836. [PubMed: 26043869]
- [111]. Al-Fatly B, Ewert S, Kübler D, Kroneberg D, Horn A, Kühn AA. Connectivity profile of thalamic deep brain stimulation to effectively treat essential tremor. *Brain* 2019; 142:3086–98. 10.1093/brain/awz236. [PubMed: 31377766]
- [112]. de Almeida Marcelino AL, Horn A, Krause P, Kühn AA, Neumann W-J. Subthalamic neuromodulation improves short-term motor learning in Parkinson's disease. *Brain* 2019;142:2198–206. 10.1093/brain/awz152. [PubMed: 31169872]
- [113]. Liebrand LC, Caan MWA, Schuurman PR, van den Munckhof P, Figee M, Denys D, et al. Individual white matter bundle trajectories are associated with deep brain stimulation response in obsessive-compulsive disorder. *Brain Stimulation* 2019;12:353–60. 10.1016/j.brs.2018.11.014. [PubMed: 30522916]
- [114]. Irmen F, Horn A, Mosley P, Perry A, Petry-Schmelzer JN, Dafsari HS, et al. Left Prefrontal Connectivity Links Subthalamic Stimulation with Depressive Symptoms. *Annals of Neurology* 2020;87:962–75. 10.1002/ana.25734. [PubMed: 32239535]
- [115]. Li N, Baldermann JC, Kibleur A, Treu S, Akram H, Elias GJB, et al. A unified connectomic target for deep brain stimulation in obsessive-compulsive disorder. *Nature Communications* 2020; 11:3364. 10.1038/s41467-020-16734-3.
- [116]. Welter M-L, Schupbach M, Czernecki V, Karachi C, Fernandez-Vidal S, Golmard J-L, et al. Optimal target localization for subthalamic stimulation in patients with Parkinson disease. *Neurology* 2014;82:1352–61. 10.1212/WNL.0000000000000315. [PubMed: 24647024]
- [117]. Eisenstein SA, Koller JM, Black KD, Campbell MC, Lugar HM, Ushe M, et al. Functional anatomy of subthalamic nucleus stimulation in Parkinson disease. *Annals of Neurology* 2014;76:279–95. 10.1002/ana.24204. [PubMed: 24953991]
- [118]. Schilling KG, Nath V, Hansen C, Parvathaneni P, Blaber J, Gao Y, et al. Limits to anatomical accuracy of diffusion tractography using modern approaches. *Neuroimage* 2019;185:1–11. 10.1016/j.neuroimage.2018.10.029. [PubMed: 30317017]
- [119]. Thomas C, Ye FQ, Irfanoglu MO, Modi P, Saleem KS, Leopold DA, et al. Anatomical accuracy of brain connections derived from diffusion MRI tractography is inherently limited. *Proc Natl Acad Sci USA* 2014;111:16574–9. 10.1073/pnas.1405672111. [PubMed: 25368179]
- [120]. Noecker AM, Frankemolle-Gilbert AM, Howell B, Petersen MV, Beylergil SB, Shaikh AG, et al. StimVision v2: Examples and Applications in Subthalamic Deep Brain Stimulation for Parkinson's Disease. *Neuromodulation: Technology at the Neural Interface* 2021;n/a. 10.1111/ner.13350.

- First evaluation of connectomic model estimates against cortical recordings in humans
- Lead localization and pathway excitability are crucial determinates of model accuracy
- Model accuracy is superior for omnidirectional compared to directional stimulation
- Patient-specificity is important for good model performance
- General model parameters may be suitable for predicting activations across patients

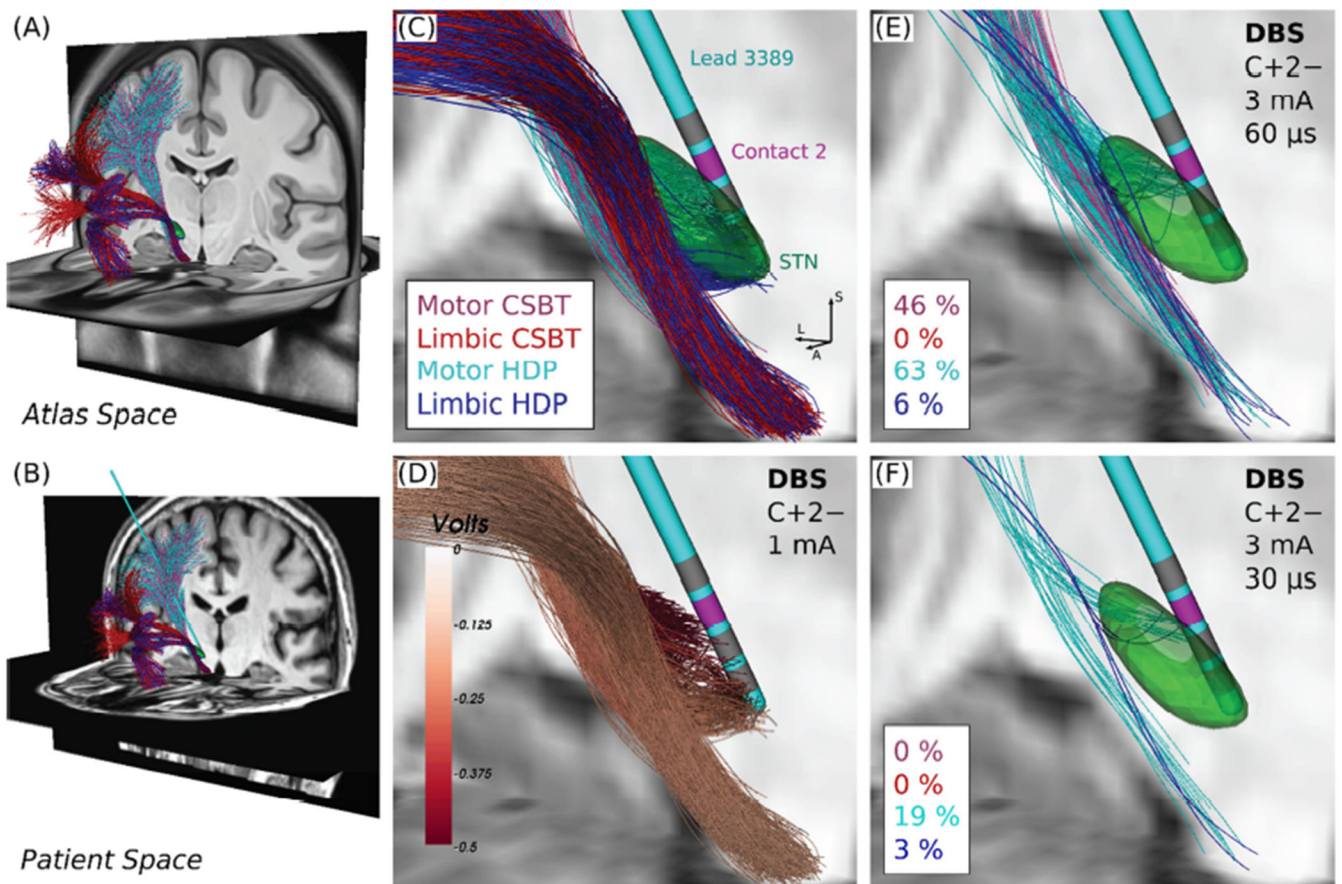


Figure 1. Individualized connectomic estimates of direct axonal activation.

(A) Anatomical models of corticospinal/bulbar tract (CSBT, *reds*) and hyperdirect pathway (HDP, *blues*) with the subthalamic nucleus (STN, *green*) overlaid. (B) Pathways warped into Patient 3's preoperative T1w space with their lead overlaid. (C) Closeup of Panel B. Directions: L = lateral, S = superior, A = anterior. (D) Extracellular voltages applied to the pathways from a 1 mA of current applied between an active cathodic contact (2-, *magenta*) and a distal large return electrode on the contralateral shoulder (C+, *not shown*). Examples of (E) percent co-activation of CSBT and HDP, and (F) selective activation of HDP at 10 Hz.

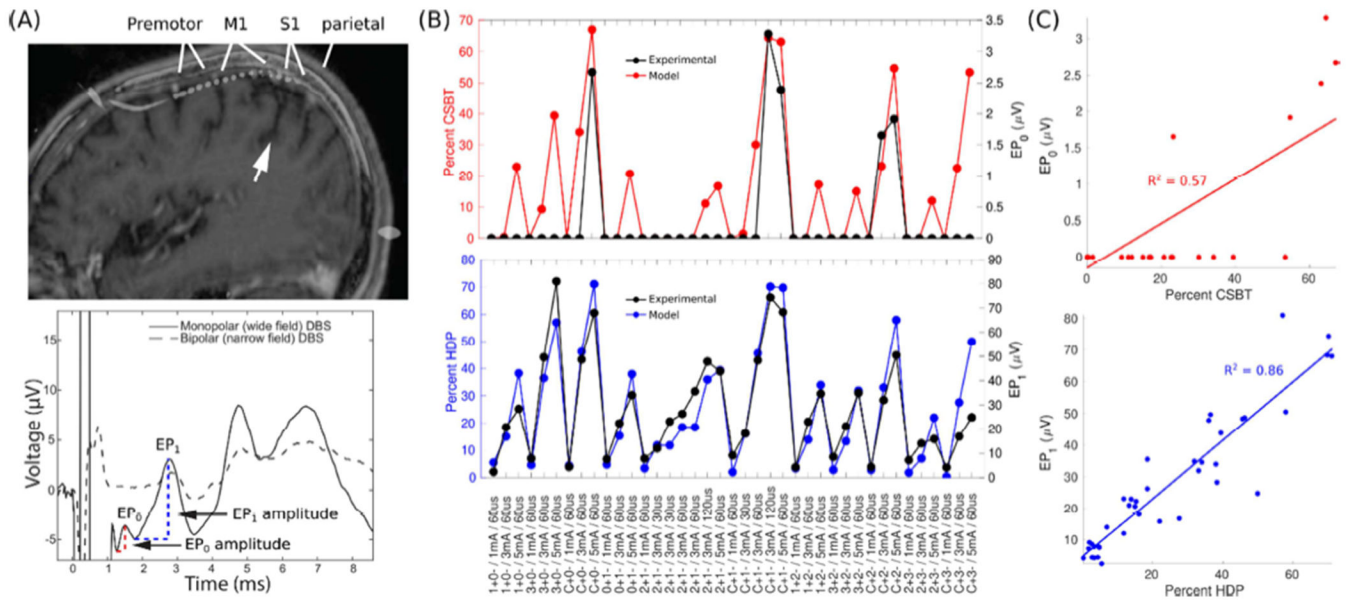


Figure 2. Electrocorticographical evaluation of direct axonal activation.
 (A) Evoked potentials (EPs) recorded with subdural electrocorticography (ECoG) during subthalamic deep brain stimulation (DBS). The electrode strip spanned the premotor cortex, primary motor cortex (M1), primary sensory cortex (S1), and superior parietal lobule. White arrow points at the central sulcus. The bottom panel depicts an averaged EP trace for monopolar and bipolar electrode configurations, demonstrating that EPs are distinct from the stimulation artifact. EP₀ and EP₁ peaks are denoted. (B) EP₀ amplitude was correlated with modeled activation of the corticospinal/bulbar tract (CSBT, *red*) and EP₁ amplitude with the hyperdirect pathway (HDP, *blue*). Data from Patient 3. (C) Linear correlations between the EPs and the model pathway activation from Panel B. R² = Coefficient of Determination. Stimulation settings: IDs of anode (+) and cathode (-) / current amplitude / stimulus pulse width. Contact 0 is nearest to the tip of Medtronic Lead 3389.

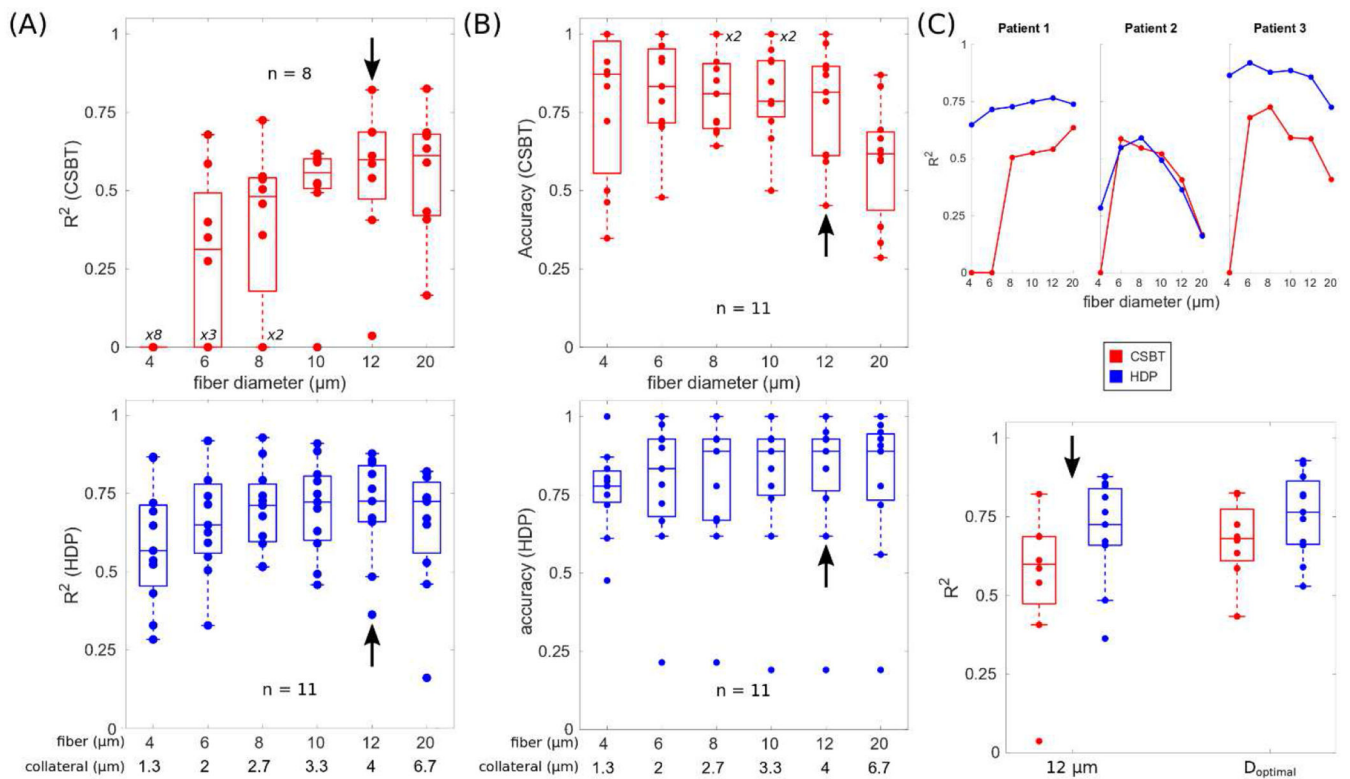


Figure 3. Model performance improved with increasing fiber diameter.

(A) Linear variation in evoked potential (EP) amplitudes explained by respective estimates of pathway activation. R^2 = coefficient of determination, CSBT = corticospinal/bulbar tract, and HDP = hyperdirect pathway with a diameter ratio of collateral to body of 1:3. (B) Accuracy in predicting activation (true positives) versus no activation (true negatives). Black arrows point to the median fiber diameter. (C) Top: individual examples of model performance by diameter and patient. Bottom: model performance with a general fiber diameter (12 μm , *black arrows*) compared to model performance when the optimal diameter was selected per patient (D_{optimal}). Patients 7, 10, and 11 are excluded ($n = 8$) for CSBT cases because their EP_0 was zero and unvarying, so R^2 was indeterminate.

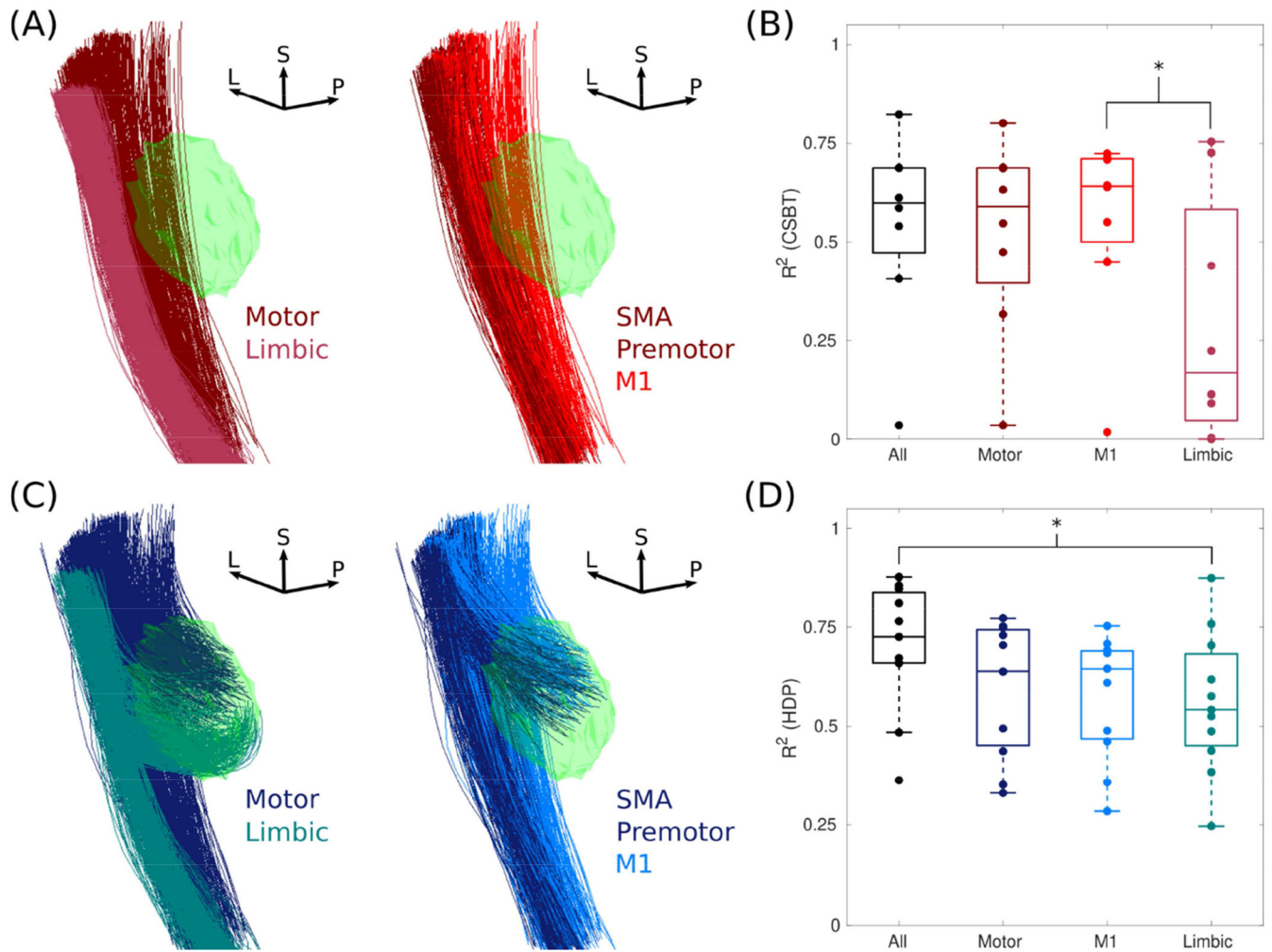


Figure 4. Model performance was optimal with all anatomical subdivisions.

(A) Anatomical subdivisions of the corticospinal/bulbar tract (CSBT, *reds*) and (B) the respective model performance using these subdivisions. Subthalamic nucleus (*green*). R^2 = coefficient of determination, L = lateral, P = posterior, and S = superior. ‘All’ is the combination of motor and limbic subdivisions (*left*), and the motor subdivision is further subdivided into the primary motor cortex (M1), supplementary motor area (SMA), and premotor cortex (*right*). (C and D) The same as A and B except for the hyperdirect pathway (HDP, *blues*). Asterisks denote statistical differences with a Kolmogorov-Smirnov test ($\alpha = 0.05$). Note, Patients 7, 10, and 11 are excluded ($n = 8$) for CSBT cases because their EP_0 was zero and unvarying, so R^2 was indeterminate.

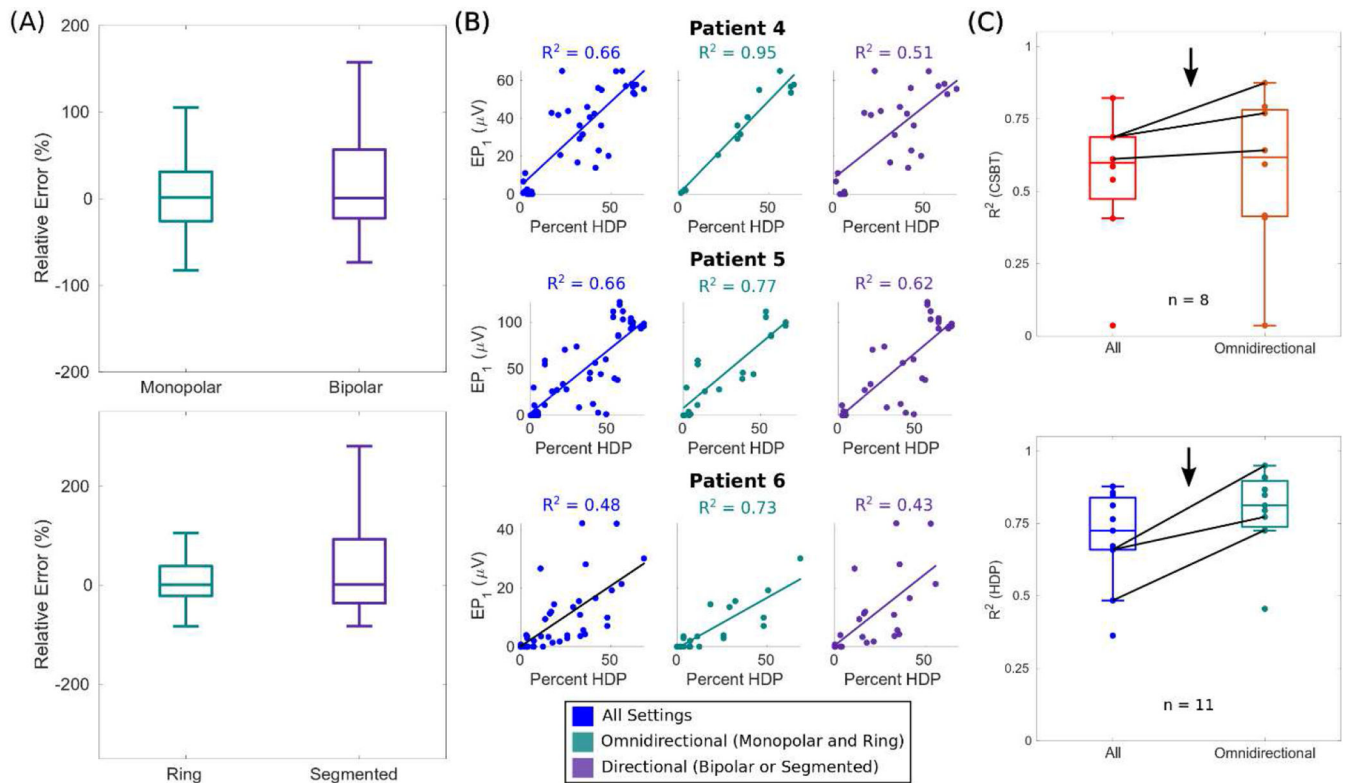


Figure 5. Model errors were minimal with omnidirectional stimulation of pathways.

(A) Relative errors ($(\text{predicted value} - \text{actual value}) / \text{actual value}$) of evoked potential 1 (EP₁) collapsed across patients, and subdivided by electrode configuration (*top*) or type (*bottom*). (B) Model fits in patients with directional leads using all data (*left*), only data acquired during omnidirectional stimulation with a monopolar, ring electrode (*middle*), or only data acquired during directional stimulation with bipolar or segmented electrodes (*right*). R² = coefficient of determination. (C) Comparative model performance with only data from omnidirectional stimulation cases. Data from patients in B are emphasized (*black arrow and lines*). R² were indeterminate for CSBT in Patient 7, 10, and 11 because EP₀ was zero for all of their settings.

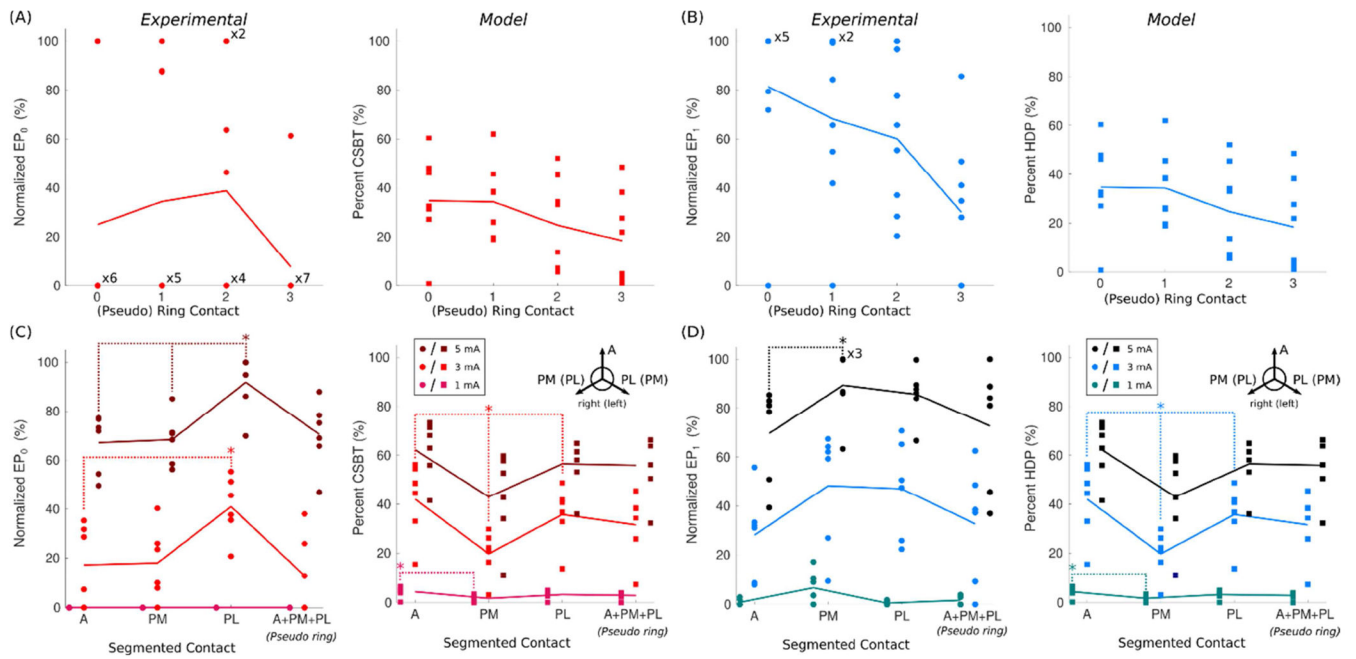


Figure 6. Evoked potential (EP) amplitudes were maximal in the posterior STN.

(A) Variation in EP₀ (circles) and estimates of corticospinal/bulbar tract (CSBT) activation (squares) at 3 mA across the four (pseudo-)ring contacts in monopolar cathodic configurations. (B) The same as Panel A except for EP₁ and the hyperdirect pathway (HDP). (C and D) Similar to A and B, except for segmented contacts at three current amplitudes. Contact orientations: A = anterior, PM = posteromedial, PL = posterolateral, with PL and PM flipped across hemispheres. The six points per each combination of orientation and amplitude are the data collected from the two segmented contacts in Patients 4–6 with steerable DBS leads. Data from Patients 7, 9, and 11 are excluded ($n = 8$) because their data were only collected with bipolar contact configurations. Bonferroni corrections were applied to the Kolmogorov-Smirnov tests to account for multiple comparisons: $\alpha < 0.05 / 6$ for A and B (4 rings choose 2) and $\alpha < 0.05 / 3$ for C and D (3 segments choose 2).

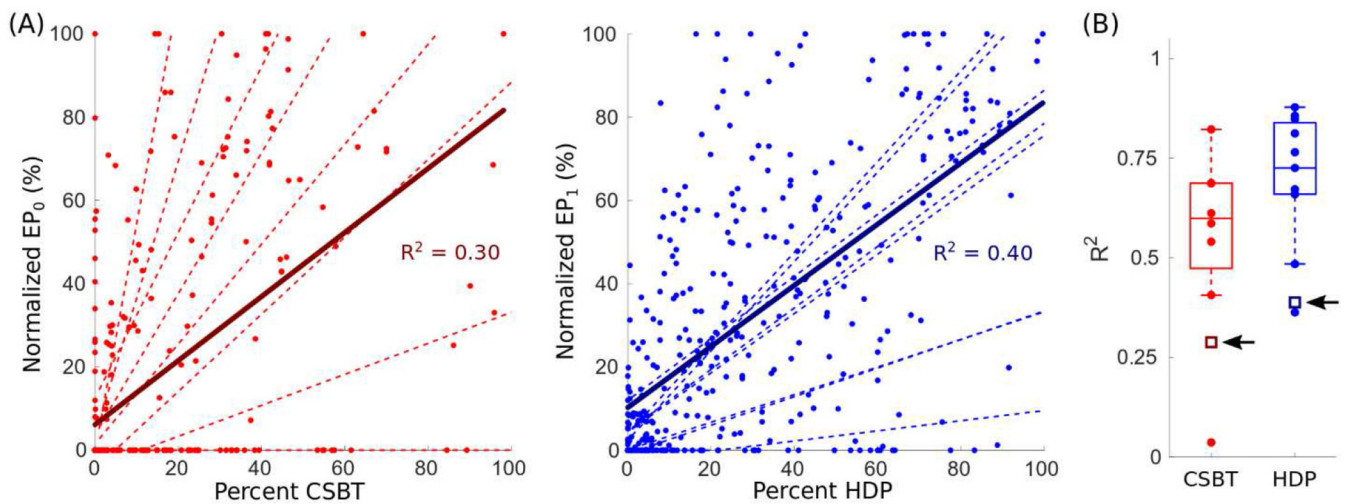


Figure 7. Patient-specificity was necessary for good model performance.

(A) Linear correlations between the normalized evoked potential (EP) amplitudes and their respective pathway activations aggregated across the entire cohort, where EP₀ (*reds*) and EP₁ (*blues*) were normalized by the respective range of amplitudes in each patient (i.e., (value – minimum value) / range of values) and expressed as a percentage. For comparison, the distribution of individual linear regression fits (*dashed lines*) for all patients are shown. R^2 = coefficient of determination, CSBT = corticospinal/bulbar tract ($n = 8$, *left*), and HDP = hyperdirect pathway ($n = 11$, *right*). (B) R^2 for aggregate fits (*open squares*) compared to respective patient-specific fits (*filled circles*). The black arrows point to the respective R^2 for aggregate fits.

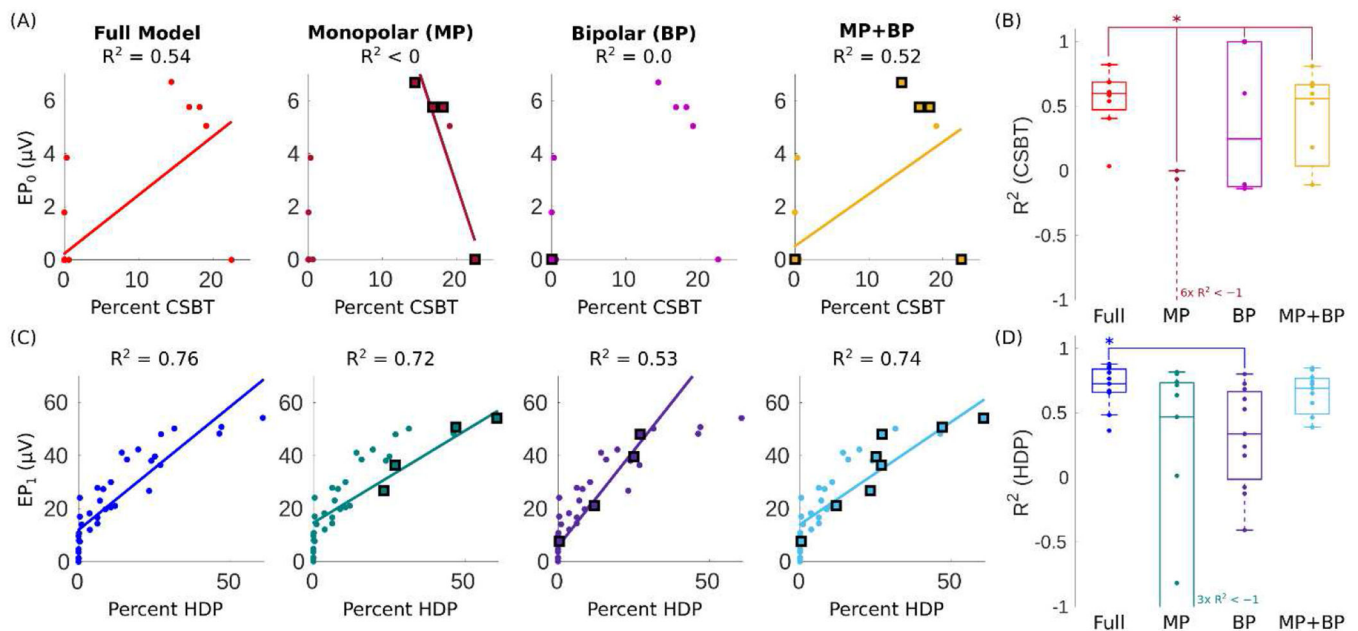


Figure 8. Eight standard ring settings explained the majority of variance in EP amplitudes. Correlations between CSBT and the respective evoked potential (EP₀) amplitude for (A) Patient 1 and (B) all patients using all stimulation settings (*red*), only four monopolar ring electrode configurations (C+0-, C+1-, C+2-, and C+3-, *maroon*), only four bipolar ring configurations (1+0-, 2+1-, 3+2-, and 2+3, *pink*), or both monopolar and bipolar ring settings combined (*gold*). For restricted cases, the regression model was fit to only four or eight settings (*enlarged and outlined in black*), and then the coefficient of determination (R^2) was calculated for all points. Pulse width = 60 μ s, and amplitude = 5 mA unless specified otherwise (see Sources of variance). For electrode configurations, C, +, and - denote stimulation case, anode, and cathode, respectively. (C–D) The same as A–B for EP₁ and HDP, with the same stimulation setting for the full (*blue*) and restricted models (*teal, purple, and cyan*). CSBT = corticospinal/bulbar tract (n = 8), and HDP = hyperdirect pathway (n = 11). Asterisks denote statistical differences with a Kolmogorov-Smirnov test ($\alpha = 0.05$).

Table 1.

Patient characteristics

Patient	Age/Sex	Center	ECoG side*	ECoG laterality at M1*, mm	DBS lead model*	Lead type	Stimulator used	No. DBS Settings
1	62/M	Emory	R	34.0	MDT 3389	Standard	Neuro Omega	36
2	53/M	Emory	R	40.9	MDT 3389	Standard	Neuro Omega	42
3	57/M	Emory	R	24.3	MDT 3389	Standard	Neuro Omega	39
4	44/M	Emory	R	18.9	ABT 6172	Steerable	Neuro Omega	42
5	53/M	Emory	R	28.0	BSC 2202	Steerable	Neuro Omega	54
6	60/M	Emory	L	26.5	ABT 6172	Steerable	Neuro Omega	46
7	64/M	UCSF	R	35.0	MDT 3389	Standard	MDT analog	18
8	65/M	UCSF	R	44.0	MDT 3389	Standard	Neuro Omega	34
9	60/M	UCSF	R	41.5	MDT 3387	Standard	MDT digital	18
10	69/M	UCSF	R	27.5	BSC 2201	Standard	Neuro Omega	27
11	67/M	UCSF	R	22.6	MDT 3387	Standard	MDT digital	20

* L (left), R (right), M1 (primary motor cortex), MDT (Medtronic), ABT (Abbott Laboratories), BSC (Boston Scientific Co.).